Low-temperature thermochronology data from the eastern South China Block decipher episodic subduction of the Paleo-Pacific Plate

Jinghua Wu [1, 2], Huan Li [1, *], Martin Danišík [3], Kotaro Yonezu [2], Han Zheng [1], Zhihan Li [1]

[1]Key Laboratory of Metallogenic Prediction of Nonferrous Metals and Geological Environment Monitoring, Ministry of Education, School of Geosciences and Info-Physics, Central South University, Changsha 410083, China

[2]Department of Earth Resources Engineering, Faculty of Engineering, Kyushu University, Fukuoka 819-0395, Japan

[3]John de Laeter Centre, Curtin University, Bentley 6845, Australia

Corresponding author: Huan Li (lihuan@csu.edu.cn)

Key Points:

- First ZHe and AHe data spanning the intracontinental eastern South China Block (SCB).
- Three-stage eastern SCB exhumation occurred from the Jurassic to the Eocene.
- Thermochronological map favors regional exhumation triggered by subduction.

Plain Language Summary

The eastern South China Block (E-SCB) is characterized by extensively outcropped Mesozoic magmatic rocks. The Mesozoic subduction of the Paleo-Pacific

Ocean was suggested to be responsible for the remarkable exhumation. Since existing hypotheses lack detailed temporal constraints on the tectonism, timing, style, and evolution of this oceanic subduction remains enigmatic. Low thermochronology enables constructing precise geochronological framework of outcropped rocks to connect with undersurface plate tectonics. However, exhumation history of the E-SCB, especially in the far hinterland, is poorly constrained and variably interpreted. To determine the subduction process, we first report zircon and apatite (U-Th/He) dating results of eight Mesozoic magmatic rocks in the intracontinental E-SCB and reveal detailed thermal history by inverse modelling. In addition, regional magmatism, structure, and low thermochronology data were collected to map their temporal and spatial patterns over time. Our results construct a precise geochronological framework of the oceanic subduction and reveal a migration of exhumation center from the intracontinental E-SCB to the epicontinental E-SCB over time. The propagation of exhumation events is consistent with advance and retreat of the oceanic subduction. This therefore indicates that the subduction of the Paleo-Pacific Ocean greatly impacted the tectonic, topographic, and climatic transitions of the E-SCB.

Abstract

Mesozoic subduction of the Paleo-Pacific Plate triggered intense tectonism, magmatism, and metallogeny in the eastern South China Block (E-SCB) and set off long-term tectonic, topographic, and climatic responses. However, contrasting hypotheses have been proposed to interpret the timing, style, and evolution of this oceanic subduction. Unraveling the exhumation history of the E-SCB is crucial to understanding deep subduction processes. To address the poorly documented exhumation history of the E-SCB, we present first zircon and apatite (U-Th)/He dates from eight Mesozoic granitoids distributed in a lateral profile across the intracontinental E-SCB. These data are combined with a compilation of regional thermochronological data, in order to address the evolution of the E-SCB in a tectonic,

topographic, and climatic evolution framework. Zircon and apatite (U-Th)/He central ages of the investigated plutons range from 146–30 Ma and 82–31 Ma, respectively, implying long-lived exhumation of the intracontinental E-SCB. Inverse thermal modelling indicates the intracontinental SCB underwent multi-phase exhumation events from the Jurassic, despite variable onset timing and the fact that the far intracontinental E-SCB had been an exhumation center prior to the Early Cretaceous. In addition, a compilation map of regional thermochronological data reveals propagation of the exhumation center from the intracontinental to the epicontinental E-SCB over time (from the Cretaceous to the Paleogene). Based on these results, we propose a refined model of Paleo-Pacific Plate subduction since the Triassic. This model is in good agreement with geological observations in the E-SCB and capable of explaining regional magmatism, metallogeny, tectonism, and exhumation.

1 Introduction

The eastern South China Block (E-SCB) was greatly influenced by northwestward subduction of the Paleo-Pacific Plate during the Mesozoic. This oceanic subduction triggered intensive magmatism, large-scale tectonism (e.g., extensional basins, magmatic domes, and strike-slip faults), and the formation of voluminous magmatic-hydrothermal deposits (Zhou et al., 2000; Mao et al., 2013; Li et al., 2014, Cao et al., 2021). Many studies have focused on E-SCB Mesozoic magmatism, structure, and metallogeny (Zhou et al., 2000; Li and Li, 2007; Jiang et al., 2009; Shu et al., 2009; Mao et al., 2013; Li et al., 2014, 2016, 2017; Gao et al., 2017; Liu et al., 2020b; Cao et al., 2021), however, there is still no agreement on the timing and style of Mesozoic tectonic evolution in the E-SCB, with current hypotheses including: (1) a change in the angle of subduction from the Early Jurassic (Zhou & Li, 2000); (2) flat-slab subduction since the Late Permian (Li & Li, 2007), and (3) advancing and retreating oceanic subduction initiated in the Jurassic (Jiang et al., 2009, 2015). These tectonic models were established from magmatic, isotopic, structural, and sedimentary perspectives, and have succeeded in interpreting many of

the geological phenomena in the E-SCB. Nevertheless, evidence incompatible with the proposed models have been increasingly reported. For example, a lack of Triassic arc magmatism in the E-SCB favors the onset of oceanic subduction later than the Triassic (Shu et al., 2008; Gao et al., 2017). In addition, a lack of clarity around the timing of Mesozoic tectonism in the E-SCB (e.g., formation ages of syntectonic basins and faults), could lead to misinterpretation of the geological evidence. In fact, this lack of temporal constraint has long vexed understanding of Paleo-Pacific Plate oceanic subduction processes.

Extensively outcropped plutonic rocks elucidate a remarkable exhumation of the E-SCB from the Mesozoic. Since exhumation events are a crustal-scale response to plate tectonics, low-temperature thermochronology provides a tool for placing temporal constraints on the interplay between the crust and deep subduction process. To date, this method has been extensively applied in topographical reconstruction (e.g., Glotzbach et al., 2011; Guillaume et al., 2013; Käßner et al., 2020; Stalder et al., 2020), climate evolution (Deng et al., 2018; Margirier et al., 2019), and structural deformation (Brady, 2002; Clark et al., 2010; Moser et al., 2017). The low-temperature thermochronological evolution of the E-SCB, particularly in the intracontinental regions, is less well-documented, which makes it difficult to assess the existing tectonic models (Chen et al., 2020; Wang et al., 2020; Sun et al., 2021). In addition, the Mesozoic exhumation history of the E-SCB has been variably interpreted (Li et al., 2016b; 2017; Su et al., 2017). A comprehensive thermochronological study of the E-SCB is vital to resolution of these issues.

In this contribution, we first present zircon and apatite (U-Th)/He (ZHe and AHe, respectively) dates from eight Mesozoic (mainly Late Jurassic) granitoids laterally distributed across the intracontinental E-SCB. This study aims to reveal the exhumation history of intracontinental E-SCB since the Jurassic, determine the tectonic cause of phased exhumation, and probe into Paleo-Pacific Plate subduction processes. Finally, a reconstruction of the thermal history using inverse modelling and a compilation of all data in regional thermochronological maps are undertaken to

provide new insights into the tectonic, climatic, and topographical evolution of the E-SCB.

2 Geological setting

The South China Block (SCB) is flanked to the east by the Pacific Plate, to the north by the North China Craton, to the southwest by the Indochina Block, and to the west by the Tethyan–Himalayan tectonic belts (Figure 1a). During the Neoproterozoic Jiangnan Orogeny, the Yangtze Block and the Cathaysia Block were amalgamated and formed a rudiment of the SCB (Yao et al., 2019). The Jiangnan Orogen has been recognized as the suture zone, with its southeastern margin defined by the lithosphere-scale Jiangshan–Shaoxing fault. Its northwestern margin and southwestern extension are not delineated by any surface feature (Figure 1a). The Yangtze Block is characterized by widespread Neoarchean basement, northern Kongling Mesoarchean complexes, and varied Neoproterozoic magmatic rocks (Xia et al., 2012; Yu et al., 2012). In contrast, Precambrian rocks of the Cathaysia Block are dominantly of Meso–Neoproterozoic age, with local outcrops of Paleoproterozoic rocks in the Zhejiang and Fujian provinces (e.g., the Badu complexes, Cawood et al., 2018; Yao et al., 2019). Due to the vast expanse of the SCB (~1,841,000 km^2), Phanerozoic tectonism, sedimentation, and magmatism are varied in the eastern and western sides of the Jiangnan Orogen (i.e., E-SCB and W-SCB), with the former tectonically influenced by multiple plates and the latter belonging to the Tethys–Himalayan tectonic regime (Shu et al., 2008; Wang et al., 2013). Phanerozoic orogenic events in the E-SCB include the Early Paleozoic intracontinental orogeny, Triassic continental collisions, and Jurassic–Cretaceous subduction of the Paleo-Pacific Plate, with ongoing debate around the timing and geodynamic mechanisms related to each (Shu et al., 2014; Gao et al., 2017). The Early Paleozoic orogeny was characterized by extensive absence of Silurian sedimentary rocks, greenschist facies metamorphism and deformation of pre-Silurian strata, and granitoid-dominated magmatism (Shu et al., 2014; Song et al., 2015). The Triassic orogeny produced large-scale ductile shear

deformation, thrust faults, folds, and granitic magmatism, with locally developed medium- to high-grade metamorphism (Faure et al., 2016; Li et al., 2016a; Gao et al., 2017). The Jurassic–Cretaceous orogeny gave rise to voluminous magmatism, intensive structural deformation, and massive polymetallic mineralization (e.g., W, Sn, Mo, Bi, Cu, Au, Pb, Zn, U, REEs, Nb, Ta, Rb, Cs), which have been investigated for decades (Li & Li, 2007; Jiang et al., 2009; Wang et al., 2013; Shu et al., 2014; Mao et al., 2013, 2021). Induced by multi-stage tectonism, the current topography of the E-SCB is basin and range (Figure 1b).

Mesozoic sedimentary rocks of the E-SCB are distributed in small- to medium-scale basins, in which Cretaceous sedimentary rocks dominate (Figure 1a). Sediments are subdivided into four groups according to stratigraphic unconformities (i.e., the Upper Triassic–Lower Jurassic strata, the Middle Jurassic strata, the Lower Cretaceous strata, and the Upper Cretaceous strata) (Li et al., 2014, 2021). The Upper Triassic–Lower Jurassic strata are fluvio–lacustrine facies and consist of conglomerate, sandstones, siltstone, and carbonaceous mudstone, with coal-bed intercalations (Shu et al., 2009). The Middle Jurassic strata are composed of fluvial-facies terrestrial clastic rocks (e.g., sandy gravel, sandstone, greywacke, and conglomerate) and bimodal volcanic rocks (e.g., basalt and rhyolite) (Shu et al., 2009). The Lower Cretaceous strata is a set of volcanic and sedimentary rocks, varied in lithologic composition in the intra- and epicontinental E-SCB, including siltstone, sandstone, mudstone, rhyolite, tuff, and basalt intercalations (Wang et al., 2013; Li et al., 2014). The Upper Cretaceous strata comprise red-colored terrestrial clastic rocks such as sandstone, siltstone, mudstone, and a gypsum-bearing layer containing many fossils (Wang et al., 2013). In addition, Paleogene strata are also present and composed of coarse fragmentary rocks, siltstone, and mudstone, with intercalated gypsum and oil-bearing shale (Shu et al., 2009; Li et al., 2021).

The E-SCB is structurally characterized by map-scale Triassic WNW-striking faults, folds and thrusts, and NE- striking ductile shear zones (Wang et al., 2021). These structures manifest NNE–SSW crustal shortening related to the Early Triassic

continental collision between the SCB and the Indochina Block, followed by collision with the North China Craton (Li et al., 2017). Jurassic to Cretaceous tectonism includes NE/NNE-trending folds, normal or strike-slip faults, and syntectonic extensional basins, which were byproducts of oceanic subduction of the Paleo-Pacific Plate (Li et al., 2017). Structural analyses have revealed multi-stage compressional and extensional events during the Jurassic, through to the Cretaceous (Li et al., 2014; Chu et al., 2019).

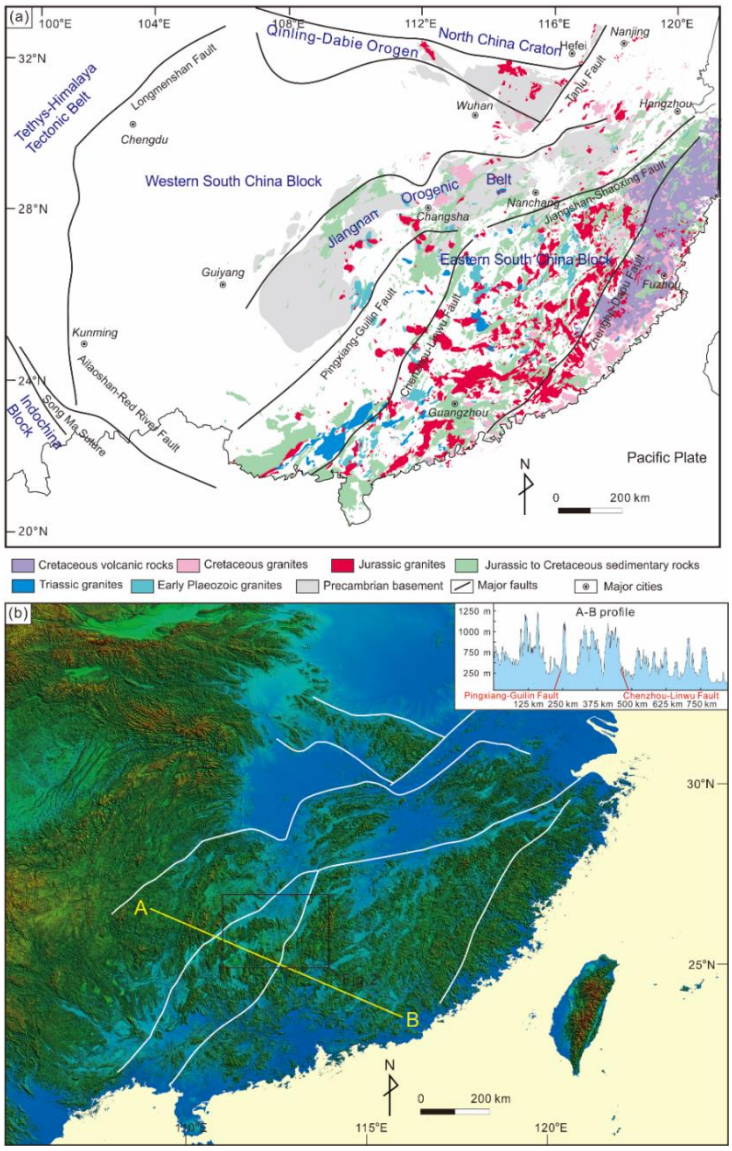

Figure 1. (a) Simplified geological map of the South China (modified from Wang et al., 2013); (b) 90 m digital elevation map of the south China (http://www.gscloud.cn/home).

Mesozoic magmatic rocks are widespread in the E-SCB, with crystallization ages ranging from the Triassic to the Cretaceous. Triassic magmatic rocks are mostly I- and S-type granitoids, located in the intracontinental E-SCB, with minor A-type granitoids identified in the epicontinental E-SCB (Gao et al., 2017). These granitoids were emplaced throughout the Triassic, peaking at 240–220 Ma, and are primarily associated with multiple continental collisions between the SCB and other plates (Gao et al., 2017). In contrast, Jurassic magmatic rocks vary in lithology from felsic to mafic, such as granite, syenite, granodiorite, granitic porphyry, diabase, and gabbro, with some bimodal volcanic rocks. Jurassic granitoids have been intensively studied and can be petrogenetically divided into I-, S-, and A-types as a result of remelting of inhomogeneous crustal basement with different degrees of mantle-derived contribution (Wang et al., 2003; Li et al., 2021). Many Jurassic granitoids (particularly those of Middle to Late Jurassic age), have a genetic relationship with nonferrous polymetallic mineralization in the world-class Nanling Ore Belt. Jurassic mafic rocks are sparsely distributed and include two groups with asthenospheric mantle-derived and lithospheric mantle-derived origin (Wang et al., 2003; Meng et al., 2012). The latter were sourced from an enriched mantle, metasomatized by slab-released fluid/melt, indicative of a potential onset of oceanic subduction from the Jurassic (Meng et al., 2012). Cretaceous magmatic rocks, typified by intensive arc-related rocks in the epicontinental E-SCB, have been related to the subduction of the Paleo-Pacific Plate. They share a similar lithology with Jurassic magmatic rocks but increasingly show an arc signature over time. Chronologically, they were emplaced from 145 Ma to 85 Ma, with two peak episodes at ~132 Ma and ~98 Ma, respectively (Li et al., 2021).

3 Sampling and analytical methods

A total of 102 zircon and 23 apatite (U-Th)/He analyses were conducted on eight Mesozoic granitoid plutons in the intracontinental SCB, constituting a lateral transect across the Chenzhou–Linwu Fault (Figure 2). For some individual granitoid plutons, samples were collected to constitute a vertical elevation profile including the Tongshanling, Baoshan, Qitianling, and Wangxianling plutons. Detailed sample locations and information are summarized in Table 1.

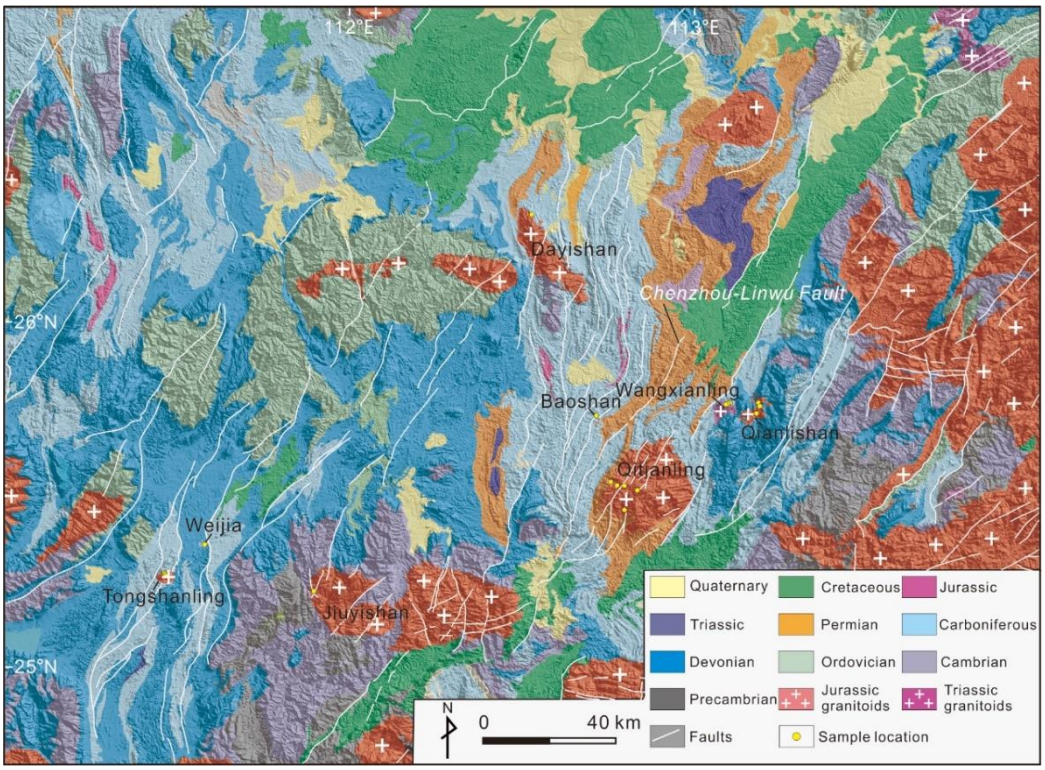

Figure 2. Geological map of the investigated area.

3.1 Zircon and apatite (U-Th)/He dating

Mineral separation was carried out in the Rock–Mineral Preparation Lab, Central South University. The whole rock samples were crushed using a ball mill, sieved to 75-200 μm fraction and separate for heavy minerals using a table concentrator. Euhedral zircon and apatite grains were selected and carefully examined under a high-power microscope. Euhedral inclusion-free zircon and apatite crystals

were packaged in and niobium and platinum microtubes, respectively, for further (U-Th)/He dating analysis.

Helium dating analysis were conducted at the (U–Th)/He Laboratory of the Institute of Geology and Geophysics and in the Low Temperature Thermochronology Facility, John de Laeter Centre, Curtin University. An automatic He analysis system (Alphachron MK II; Australian Scientific Instruments, ASI) with a 970 nm diode laser was used to extract ^{4}He from mineral crystals at temperature of 900 °C for 5 minutes (apatite) or 1250 °C for 15 minutes (zircon). This process was repeated to ensure total extraction of 99% of the available ^{4}He. In addition, the system uses two getters (SAES AP-10-N) to purify gas. Isotopic analyses were performed using a mass spectrometer (Quadruple Prisma Plus QMG 220). Two tanks with known amount of ^{4}He and ^{3}He were applied to calculate the ^{4}He content of each sample using isotope dilution.

After ^{4}He extraction, PFA vials were used for apatite dissolution according to the procedure of Evans et al. (2005). 25 µl of spike solution ^{235}U and ^{230}Th was added to the vials which were ultrasonicated for 15 min and then left for ~4 h at room temperature to ensure complete dissolution. A total of 325 µl of Milli-Q water was added to dilute the solutions to 350 µl for U-Th analysis on inductively coupled plasma-mass spectrometry (ICP-MS).

A spike solution prepared with 350 µl of HF and 25 µl of ^{235}U-^{230}Th spike was used to digest niobium-wrapped zircon grains in PFA vials. Three sets of vials which contain samples, blanks (a piece of Nb foil), and a spiked standard (a piece of Nb foil plus spike solution) were prepared and heated in Parr bombs to 240 °C for 36 h. Once the Parr bombs cooled to room temperature, the vials were placed on a hot plate at 70 °C for ~48 h to evaporate the HF + spike solution and enable the precipitation of fluoride salts. Consequently, 350 µl and 9 ml of HCl were added to the Parrish vials and the liner, respectively, which were then returned to the Parr bomb and heated at 200 °C for 24 h. The solutions were evaporated down to 50 µl, diluted with 300 µl of Milli-Q water (with < 0.3% wetting agent), and then transferred to 2 ml conical-base

Teflon vials, ready for U-Th analysis on ICP-MS.

Standards including Fish Canyon zircon (dated at 28.3 ± 2.6 Ma; Reiners, 2005) and Durango apatite (31.5 ± 1.0 Ma, Evans et al., 2005) were used to monitor the analytical procedure. The weighted mean (U-Th)/He dates were of 28.5 ± 0.5 Ma (n = 9) and 31.2 ± 0.7 Ma (n = 7) Ma for the measured Fish Canyon zircons and Durango apatites, respectively, consistent with recommended values within error (Table S1).

Table 1. Sample information

Sample No.	Lithology	Elevation (m)	Latitude and Longitude	Age (Ma)
TSL-1	Granodiorite	638	25.2750°N, 111.4619°E	166.6 ± 0.4 Ma
TSL-3	Granodiorite	723	25.2722°N, 111.4644°E	(MSWD = 0.23)
TSL-4	Granodiorite	823	25.2689°N, 111.4656°E	Kong et al., 2018
TSL-6	Granodiorite	904	25.2650°N, 111.4675°E	
WJ-1	Granite porphyry	295	A drilling hole of Weijia	158.7 ± 2.3 Ma
WJ-3	Granite porphyry	195	deposit	(MSWD = 0.78)
			25.3558°N, 111.5806°E	Kong et al., 2018
JYS-7	Granite	1028	25.2211°N, 111.8953°E	153.0 ± 0.9 Ma
				(MSWD = 0.18)
				Liu et al., 2019
DYS-1	Granite	143	26.3193°N, 112.5356°E	158.2 ± 1.2 Ma
				(MSWD = 1.2)
				Zhang et al., 2021
BS-1	Granodioritic porphyry	–150	Underground tunnels of the Baoshan deposit	167.0 ± 3.0 Ma (MSWD = 1.12)
BS-2	Granodioritic porphyry	–270	25.7300°N, 112.7144°E	Kong et al., 2018
BS-3	Granodioritic porphyry	–110		
QTL-1	Granite	684	25.5381°N, 112.7564°E	153 ± 2 Ma
QTL-2	Granite	1016	25.5275°N, 112.7753°E	(MSWD = 0.32)
QTL-5	Granite	1161	25.5269°N, 112.7961°E	Shu et al., 2011
QTL-6	Granite	1346	25.5136°N, 112.8342°E	
QTL-7	Granite	605	25.4567°N, 112.7967°E	
WXL-1	Granite	319	25.7744°N, 113.1339°E	223.5 ± 1.8 Ma
WXL-5	Granite	388	25.7708°N, 113.1042°E	(MSWD = 0.29)
WXL-6	Granite	420	25.7706°N, 113.1019°E	Zhang et al., 2015
QLS-1	Granite	276	25.7672°N, 113.1619°E	155 ± 2 Ma
QLS-2	Granite	347	25.7575°N, 113.1657°E	(MSWD = 1.19)

QLS-3	Granite	411	25.7368°N, 113.1564°E	Shu et al., 2011

3.2 Inverse thermal modeling

Inverse thermal modelling was performed using both HeFTy V1.9.0 (Ketcham, 2005) and QTQt V5.4.6 (Gallagher, 2012) software. The two programs run with different inverse modeling algorithms (Vermeesch & Tian, 2014) and the results are combined in this work to derive a more complete thermal history. Due to different sampling strategies during the fieldwork, inverse thermal modelling methods are varied for each pluton, including multi-minerals, vertical profile, and single zircon constraint methods. Specifically, multi-minerals constraint method refers to using ZHe and AHe data from the same sample to perform inverse thermal modelling. Vertical profile and single zircon constraint methods were applied to granitoid plutons with and without significant altitudinal changes, respectively. In addition, individual zircon/apatite grains that yielded a similar age to the central age of the host-sample were selected for inverse modelling. Detailed inverse modelling strategies for each pluton are shown in Table 2.

When performing QTQt inverse modelling, we set the present temperature and present geothermal gradient as 10 ± 10 °C and 30 ± 30 °C/km, respectively. Given a lack of low-temperature thermochronological information for these granitoids, zircon U-Pb ages of the investigated granitoids (Table 1), zircon U-Pb closure temperature (950 ± 50 °C, Cherniak and Watson, 2001), helium closure temperatures of zircon and apatite (180 ± 20 °C and 70 ± 20 °C, respectively; Wolf et al., 1996; Reiners et al., 2004), and a slightly larger He age span of each pluton (e.g., 75 ± 25 Ma for 56–93 Ma of the Tongshanling pluton, Table 2) were adopted as initial time-temperature constraints. All the modeling processes run with 100,000 iterations for burn-in process and 100,000 for posterior ensemble, with no obvious trend in the likelihood/posterior chain for all models. The paleo-geothermal gradient is assumed at 25 ± 5 °C for estimating exhumation rate.

Table 2. Inverse modelling strategies for the investigated plutons

Samples	(U-Th)/He age span (Ma)		Samples for inverse modelling		Time-temperature constraints
	Zircon	Apatite	Zircon	Apatite	
Tongshanling	56–93	37–60	TSL3-3	TSL3-6	950 ± 50 ℃ for 167 ± 1 Ma 180 ± 20 ℃ for 75 ± 25 Ma 70 ± 20 ℃ for 50 ± 15 Ma
Weijia	83–162		WJ1-3 WJ3-4		950 ± 50 ℃ for 159 ± 2 Ma 180 ± 20 ℃ for 120 ± 45 Ma
Jiuyishan	97–141		JYS7-5		950 ± 50 ℃ for 153 ± 1 Ma 180 ± 20 ℃ for 120 ± 25 Ma
Dayishan	44–56		DYS1-4		950 ± 50 ℃ for 158 ± 1 Ma 180 ± 20 ℃ for 50 ± 10Ma
Baoshan	116–148	42–63	BS2-6	BS2-4	950 ± 50 ℃ for 167 ± 3 Ma 180 ± 20 ℃ for 130 ± 20 Ma 70 ± 20 ℃ for 50 ± 15 Ma
Qitianling	64–103	26–36	QTL2-1	QTL2-1	950 ± 50 ℃ for 153 ± 2 Ma 180 ± 20 ℃ for 85 ± 25 Ma 70 ± 20 ℃ for 30 ± 10 Ma
Wangxianling	28–82		WXL1-1 WXL5-5 WXL6-3		950 ± 50 ℃ for 224 ± 2 Ma 180 ± 20 ℃ for 55 ± 30 Ma
Qianlishan	77–96	75–89	QLS1-4	QLS1-3	950 ± 50 ℃ for 155 ± 2 Ma 180 ± 20 ℃ for 85 ± 15 Ma 70 ± 20 ℃ for 80 ± 10 Ma

4 Results

ZHe and AHe ages are summarized in Tables S2 and S3, respectively. Isoplot R (Vermeesch, 2018) and Helioplot 2.0 (Vermeesch, 2010) software were used to generate weighted mean age and central age, respectively. A pilot calculation of central age using all the ZHe or AHe ages for each granitoid sample was performed. Weighted mean age and central age were recalculated after rejecting anomalous ages that led to high dispersion (> 15%), with the cause of dispersion discussed below. As a result, weighted mean ages and central ages of all samples are identical within error. The central age was further applied to inverse thermal modeling and following discussion as it is the most accurate representation of the average age in single-sample analyses (Vermeesch, 2008).

4.1 Zircon (U-Th)/He data

For the Tongshanling granodiorite samples (n = 4), a total of 16 zircon grains yielded ZHe ages (F_T-corrected age, the same below) ranging from 56.0 ± 3.1 to 93.4 ± 5.1 Ma (1 sigma, analytical error), with four dispersed ZHe ages older than 130 Ma (Figure 3a). For the Weijia granite porphyry samples (n = 2), 6 ZHe ages were obtained that vary from 83.2 ± 4.6 to 162.7 ± 16.8 Ma, with four significantly dispersed ZHe ages (> 180 Ma) (Figure 3b). For the Jiuyishan granite sample (n = 1), 5 ZHe ages fall between 97.0 ± 5.3 Ma and 141.0 ± 14.5 Ma (Figure 3c). For the Dayishan granite sample (n = 1), 3 ZHe ages show a narrow range of 43.6 ± 2.4 to 56.2 ± 3.2 Ma, with two dispersed ZHe ages of 74.2 ± 4.0 and 97.0 ± 5.3 Ma (Figure 3d). For the Baoshan granite samples (n = 3), 11 zircon grains were dated between 115.9 ± 6.4 Ma and 148.4 ± 8.0 Ma, with two young dispersed ZHe ages of 70.3 ± 3.8 Ma and 84.6 ± 4.7 Ma (Figure 3e). For the Qitianling granite samples (n = 5), 24 ZHe ages vary from 64.3 ± 3.5 Ma to 103.3 ± 5.7 Ma and one zircon grain yields an extremely old ZHe age of 248.9 ± 13.6 Ma (Figure 3f). For the Wangxianling granite samples (n = 3), 13 zircon grains give variable ZHe ages ranging from 28.3 ± 1.5 Ma to 82.4 ± 4.4 Ma and two zircon grains produce dispersed ZHe ages of 17.2 ± 0.9 Ma and 52.1 ± 2.9 Ma (Figure 3g). For the Qianlishan granite samples (n = 2), 8 zircon grains generate ZHe ages ranging from 77.2 ± 7.9 to 95.6 ± 5.2 Ma with one outlier (QLS2-5) of 169.5 ± 17.3 Ma (Figure 3h).

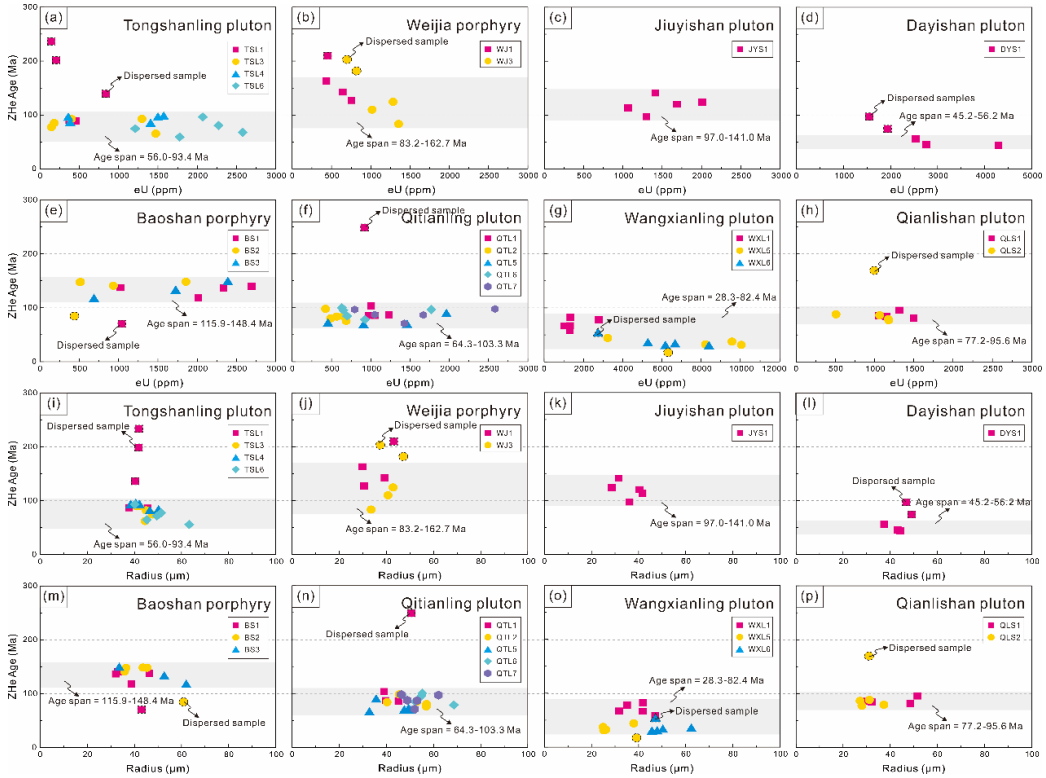

Figure 3. Plots of eU vs. ZHe age for samples from (a) Tongshanling granodiorite; (b) Weijia granite porphyry; (c) Jiuyishan granite; (d) Dayishan granite; (e) Baoshan granodioritic porphyry; (f) Qitianling granite; (g) Wangxianling granite; (h) Qianlishan granite; and radius vs. ZHe age for samples from (i) Tongshanling granodiorite; (j) Weijia granite porphyry; (k) Jiuyishan granite; (l) Dayishan granite; (m) Baoshan granodioritic porphyry; (n) Qitianling granite; (o) Wangxianling granite; (p) Qianlishan granite.

4.2 Apatite (U-Th)/He data

Many granitoids in this study are highly-evolved A-type, with low phosphorous contents. These P-unsaturated melts do not favor apatite precipitation and apatite grains were separated from four granitoid plutons only.

For the Tongshanling granodiorite sample, 6 apatite grains yielded AHe ages varying from 37.3 ± 2.5 Ma to 59.6 ± 6.3 Ma (Figure 4a). For the Baoshan granodiorite, 5 apatite grains gave AHe ages between 41.7 ± 4.5 Ma and 63.2 ± 4.1

Ma, with two dispersed AHe ages of 77.7 ± 4.7 and 108.3 ± 16.9 Ma (Figure 4b). For the Qitianling granodiorite sample, 5 apatite grains generated AHe ages of 41.7 ± 4.5 to 63.2 ± 4.1 Ma (Figure 4c). For the Qianlishan granite sample, 2 apatite grains yielded AHe ages of 75.3 ± 5.1 to 88.7 ± 5.7 Ma, with two outliers (QLS1-2 and QLS1-5) of 53.3 ± 3.2 to 119.4 ± 7.1 Ma (Figure 4d).

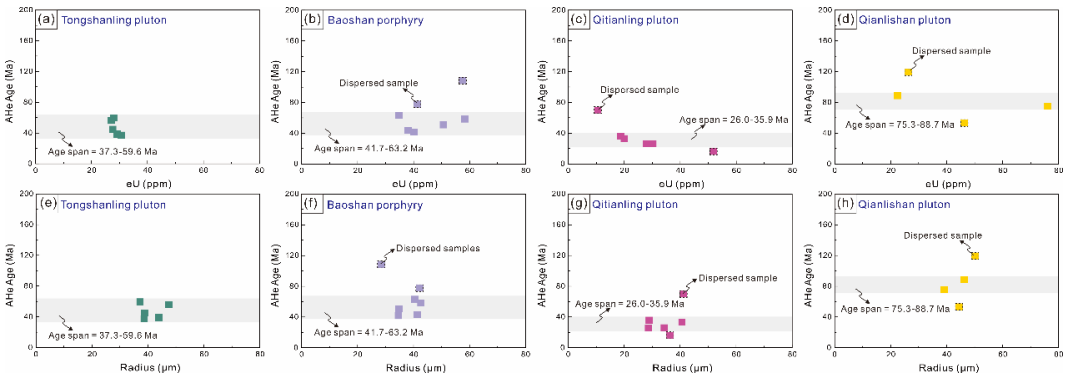

Figure 4. Plots of eU vs. AHe age for samples from (a) Tongshanling granodiorite; (b) Baoshan granodioritic porphyry; (c) Qitianling granite; and (d) Qianlishan granite.

4.3 Thermal history modelling results

The HeFTy model shows that the Tongshanling pluton experienced a three-phase cooling: (1) rapid cooling at 165–75 Ma; (2) slow cooling at 75 to 42 Ma; and (3) short and rapid cooling at 42–40 Ma (Figure 5a). The QTQt model indicates a similar but more detailed thermal history of the Tongshanling pluton beginning with rapid cooling across the ZHe partial retention zone (ZPRZ) at 167–97 Ma, residence in the AHe partial retention zone (APRZ) at 97 to 65 Ma, and quick cooling to surface temperature at 65–61 Ma (Figures 5b–c).

The HeFTy model deciphers a two-phase cooling history for the Weijia porphyry, with a rapid cooling occurring at 160–132 Ma and gradual cooling since 132 Ma (Figure 5d). Similarly, the QTQt model shows that the Weijia porphyry underwent rapid cooling at 161–158 Ma, followed by a decreased cooling rate since

158 Ma (Figures 5e–f).

Similar to the Weijia porphyry, both the HeFTy and QTQt models show a two-phase thermal history for the Jiuyishan pluton: rapid cooling at 152–112 Ma (HeFTy model, Figure 5g) or 153–142 Ma (QTQt model, Figures 5h–i), and slow cooling since 112 Ma (HeFTy model) or 142 Ma (QTQt model).

The HeFTy model shows that the Dayishan pluton experienced ~77 Myr of monotonic cooling since 155 Ma, residence in the ZPRZ at 78–46 Ma, and accelerated cooling since 46 Ma (Figure 5j). In contrast, the QTQt models suggests fast cooling at 158–80 Ma and a long residence in the ZPRZ (80 Ma to 60 Ma) with accelerated cooling to the surface since 60 Ma (Figures 5k–l).

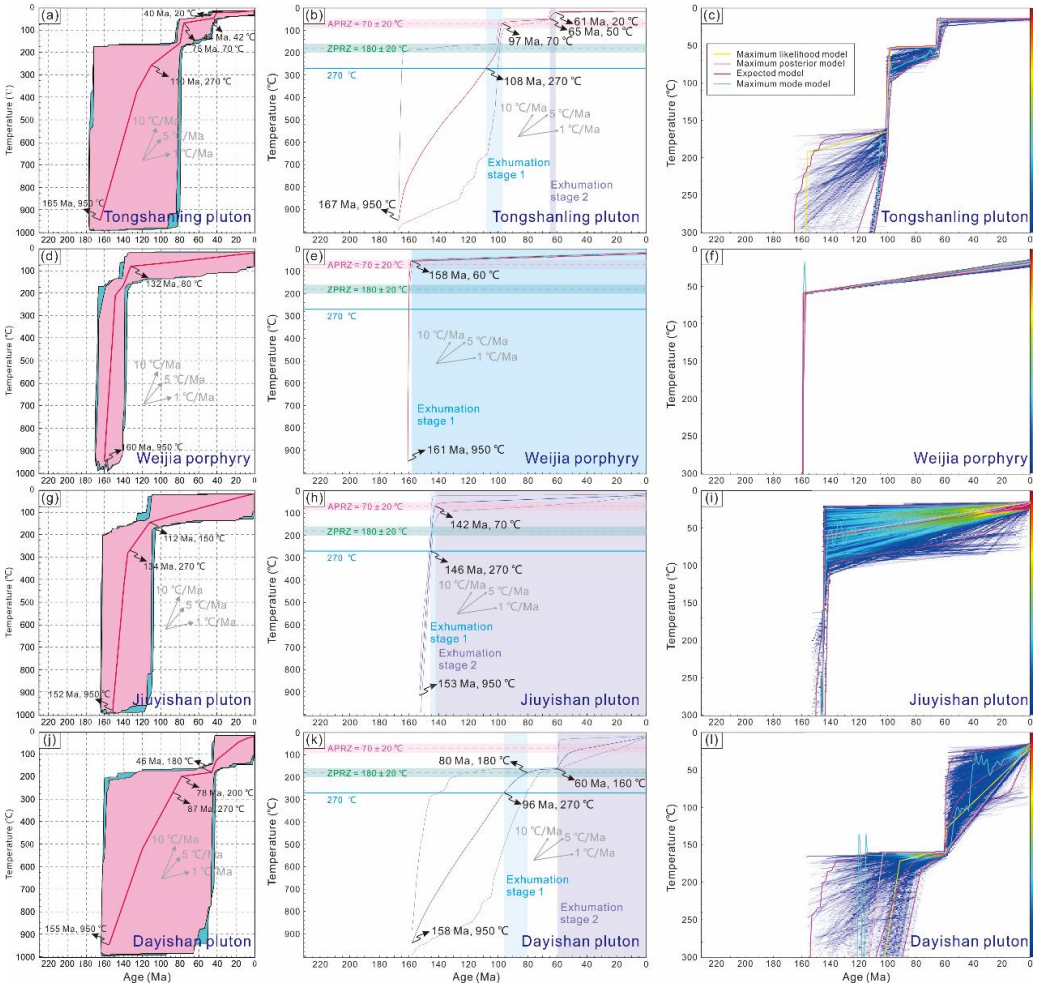

Figure 5. Inverse modelling results of the granitoids in the west of Chenzhou–Linwu Fault (a) T-t pathways of Tongshanling pluton obtained from HeFTy program; (b) expected T-t pathways of Tongshanling pluton obtained from QTQt program; (c) individual sample T-t pathways of Tongshanling pluton obtained from QTQt program; (d) T-t pathways of Weijia porphyry obtained from HeFTy program; (e) expected T-t pathways of Weijia porphyry obtained from QTQt program; (f) individual sample T-t pathways of Weijia porphyry obtained from QTQt program; (g) T-t pathways of Jiuyishan pluton obtained from HeFTy program; (h) expected T-t pathways of Jiuyishan pluton obtained from QTQt program; (i) individual sample T-t pathways of Jiuyishan pluton obtained from QTQt program; (j) T-t pathways of Dayishan pluton obtained from HeFTy program; (k) expected T-t pathways of Dayishan pluton obtained from QTQt program; (l) individual sample T-t pathways of Dayishan pluton obtained from QTQt program.

The Baoshan porphyry experienced a three-stage thermal history as revealed by two inverse models: rapid cooling (168–141 Ma of HeFTy model vs. 168–147 Ma of QTQt model), long residence in APRZ (141–58 Ma of HeFTy model vs. 147–66 Ma of QTQt model), and a rapid cooling to the surface temperature since the Late Cretaceous (58–51 Ma of HeFTy model vs. 66–63 Ma of QTQt model) (Figures 6a–c).

A three-stage thermal history is also observed in the Qitianling pluton which experienced a rapid cooling throughout the Early Cretaceous (156–96 Ma of HeFTy model vs. 155–100 Ma of QTQt model) and stayed in APRZ from the Late Cretaceous to Eocene (96–43 Ma of HeFTy model vs. 100–41 Ma of QTQt model), in the wake of a rapid cooling to the surface since the Ypresian (43–0 Ma of HeFTy model vs. 41–39 Ma of QTQt model) (Figures 6d–f).

The Wangxianling pluton experienced a complex cooling history since the Middle Triassic (~225 Ma) as suggested the HeFTy model (Figure 6g): (1) an remarkable cooling from 226 to 175 Ma, (2) a steady cooling during 175–36 Ma, and

(3) a fast cooling to the surface since 36 Ma. In comparison, the QTQt model indicates a six-phase cooling history which includes a 225–172 Ma rapid cooling, 172–102 Ma steady cooling, 102–86 Ma residual in ZPRZ, short-lived cooling (86–82 Ma), 82–59 Ma quiescence, and 59–52 Ma fast cooling to the surface (Figures 6h–i).

As shown in the HeFTy model (Figure 6j), the Qianlishan pluton underwent fast cooling from 154 to 124 Ma, resided in the ZPRZ for 42 Myr, and reached the surface at 82–76 Ma. The QTQt models indicate fast cooling at 156–133 Ma, 133–100 Ma residence in the ZPRZ, and accelerated cooling at 100–86 Ma (Figures 6k–l).

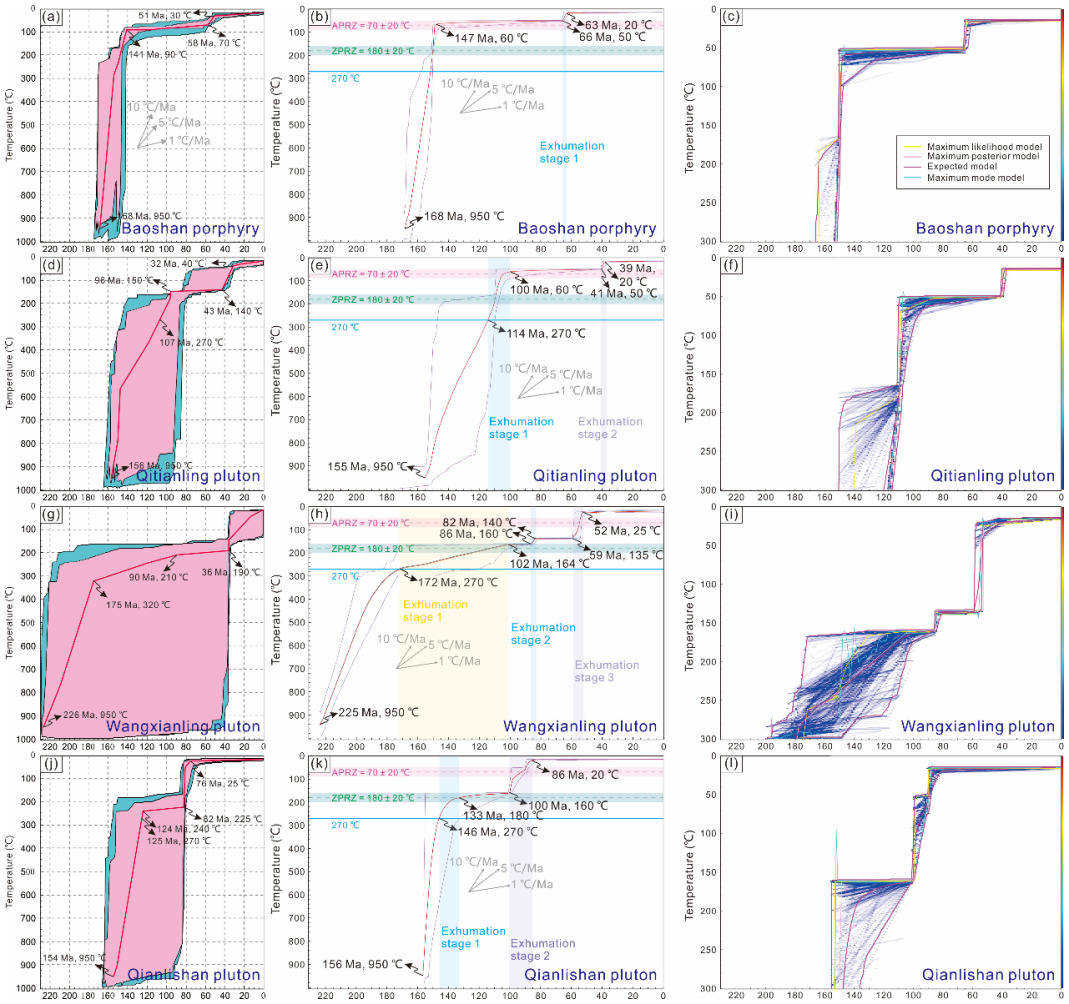

Figure 6. Inverse modelling results of the granitoids in the east of Chenzhou–Linwu Fault (a) T-t pathways of Baoshan porphyry obtained from HeFTy program; (b)

expected T-t pathways of Baoshan porphyry obtained from QTQt program; (c) individual sample T-t pathways of Baoshan porphyry obtained from QTQt program; (d) T-t pathways of Qitianling pluton obtained from HeFTy program; (e) expected T-t pathways of Qitianling pluton obtained from QTQt program; (f) individual sample T-t pathways of Qitianling pluton obtained from QTQt program; (g) T-t pathways of Wangxianling pluton obtained from HeFTy program; (h) expected T-t pathways of Wangxianling pluton obtained from QTQt program; (i) individual sample T-t pathways of Wangxianling pluton obtained from QTQt program; (j) T-t pathways of Qianlishan pluton obtained from HeFTy program; (k) expected T-t pathways of Qianlishan pluton obtained from QTQt program; (l) individual sample T-t pathways of Qianlishan pluton obtained from QTQt program.

5 Discussion

5.1 Assessment and interpretation of the (U-Th)/He data

As shown in the results (Tables S2 and S3), many samples show a wide intrasample variation of ZHe and AHe ages and which may be related to crystal size, U-Th-rich inclusiona, U-Th zonation, and radiation damage in individual crystal grains (Reiners & Farley, 2001; Brown et al., 2013; Guenthner et al., 2013; Willett et al., 2017).

Helium retention and closure temperature are elevated as the intensity of radiation damage increases (Shuster et al., 2006; Flowers et al., 2007; Gautheron et al., 2009). The damage can be numerically estimated by eU values (concentrations of effective U, defined as eU = U + 0.235 × Th in ppm). In this study, eU values do not correlate with ages, indicating that radiation damage was not the critical control on anomalously old He ages (Figures 3a–h and 4a–d). In addition, most zircon/apatite crystals analysed were of comparable size and no positive correlation was noted between He age and grain radius (Figures 3i–p and 4e–h). This suggests grain size was not a primary cause of anomalously old He ages.

Zircon and apatite grains with U-Th-enriched cores can yield anomalously old ages if zonation is not accounted for (Reiners et al., 2004). Similarly, grains with U-Th-enriched rims will yield anomalously young ages. However, date dispersion triggered by U-Th zonation are commonly 10–15% and perhaps up to 30–40% only in grains with extreme zonation (Fitzgerald et al., 2006; Ault & Flowers, 2012; Brown et al., 2013). In this study, most anomalously old He ages are pre-Oxfordian (> 160 Ma) and significantly deviate from the central ages. Often the determined age was older than the intrusive age of the host magmatic rock, except for four ZHe ages (i.e., TSL6-7, WXL6-4, DYS1-3, and DYS1-6). U-Th zonation is less likely to result in these extremely old He ages but may produce slightly dispersed young He ages such as in sample WXL5-3, BS1-3, and BS2-3. There are previous reports of zircons from this region with U-Th-enriched rims resulting from intensive hydrothermal alteration (Wu et al., 2018; Jiang et al., 2020).

Undetected U-Th-rich minerals (e.g., xenotime and monazite) or He-bearing fluid inclusions are the most likely reason for the anomalously old He ages. These tiny minerals or fluid inclusions can occur via microscopic exsolution, despite attempts to pick inclusion-free zircon/apatite grains. Most investigated granitoid plutons are highly-evolved and U-Th-rich minerals (e.g., coffinite, thorite, and uranium oxide) are widely intergrown with zircons as indicated by many studies (Li et al., 2018; Wu et al., 2018; Jiang et al., 2020). It is, therefore, most likely that the old He ages resulted from the undetected presence of inclusions enriched in parent isotopes.

Other mechanisms including zircon/apatite chemical composition, complicated thermal history, and broken crystals, may also affect He age dispersion (Crowley et al., 1991; Barbarand et al., 2003; Brown et al., 2013; Willett et al., 2017). However, there is no systematic correlation between any of these parameters and grains that yielded anomalously old ages analysed in this work.

5.2 Exhumation history of the intracontinental E-SCB since the Jurassic

Samples of the Tongshanling, Baoshan, Qitianling, and Wangxianling plutons were collected from the transect at different elevations. None of the plutons display a positive correlation between ZHe age and elevation with all displaying either no relationship or a negative correlation (Figure 7a–b). Normally, and if the variation in elevation between samples is significant, ZHe ages will positively correlate with elevation but the pattern observed here is common if the paleosurface is uneven or the geological body has been structurally deformed. Extensive Jurassic magmatism in the E-SCB led to well-developed magmatic domes and detachment faults (e.g., Mufushan, Hengshan, Wugongshan, and Lushan granitoid plutons; Li et al., 2014), and these extensional structures favor a fast exhumation of deeply-seated samples. Thus, ZHe age-elevation profiles are not applicable when defining exhumation rates in these samples.

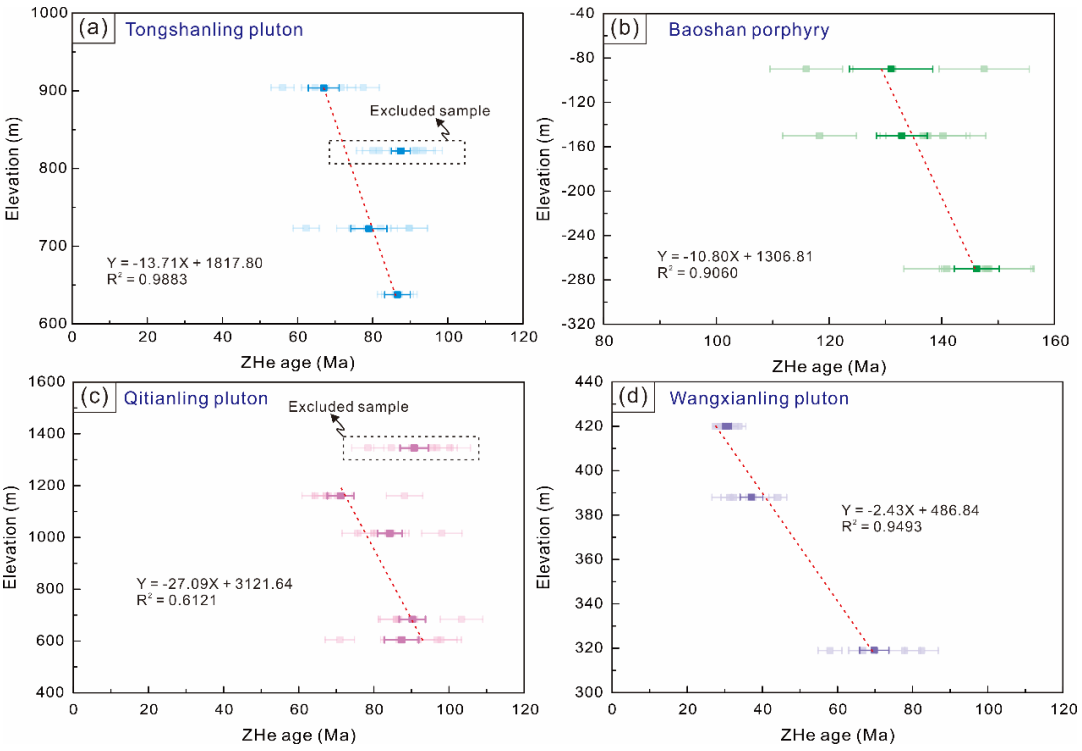

Figure 7. ZHe age vs. elevation profiles of (a) Tongshanling pluton; (b) Baoshan porphyry; (c) Qitianling pluton; and (d) Wangxianling pluton.

A consistent multi-stage thermal history for each pluton was revealed by two modelling approaches (HeFTy and QTQt). Given the additional detail provided by the QTQt model and previous work comparing the two approaches (Vermeesch & Tian, 2014), the QTQt modelling results were utilized to estimate exhumation rates in this work. Typically, the cooling history of intrusive rocks begins with an early stage of fast cooling to the subsurface ambient temperature of the host wall rocks, followed by a later stage of exhumation cooling as the intrusive is slowly exposed to the Earth's surface. Due to a lack of biotite or muscovite thermochronological constraints, the plutonic granitoids and felsic porphyries were assumed to be emplaced at 10 km depth (~270 °C) and 2 km (~70 °C), respectively (Jacob & Moyen, 2021). Thus, the long-term exhumation stage spanned 108–61 Ma for the Tongshanling pluton, 158–0 Ma for the Weijia porphyry, 146–0 Ma for the Jiuyishan pluton, 96–0 Ma for the Dayishan pluton, 147–63 Ma for the Baoshan porphyry, 114–39 Ma for the Qitianling pluton, 172–52 Ma for the Wangxianling pluton, and 146–86 Ma for the Qianlishan pluton, respectively. By assuming paleo-geothermal gradient at 25 ± 5 °C/km, long-term exhumation rates vary from 0.177–0.266 km/Myr for the Tongshanling pluton, 0.008–0.013 km/Myr for the Weijia porphyry, 0.057–0.086 km/Myr for the Jiuyishan pluton, 0.087–0.130 km/Myr for the Dayishan pluton, 0.016–0.024 km/Myr for the Baoshan porphyry, 0.111–0.167 km/Myr for the Qitianling pluton, 0.068–0.102 km/Myr for the Wangxianling pluton, and 0.139–0.208 km/Myr for the Qianlishan pluton, respectively (Table 3). However, it should be pointed out that the Weijia, Jiuyishan, Dayishan, and Wangxianling granitoids should have much higher factual exhumation rates than those given by the modelling results. This is because the four modelling results show cooling events ended until now in contrast to other granitoids with AHe age constrain (e.g., Tongshanling, Qitianling).

Table 3. Calculated parameters and results of long-term exhumation rates

Granitoids	Timing of cooling phase (Ma)	Multi-phase cooling rates (°C/Ma)	Calculated long-term exhumation rates (km/Ma)

	Stage 1 Stage 3 Stage 5	Stage 2 Stage 4	Stage 1 Stage 3 Stage 5	Stage 2 Stage 4	Inverse modelling method	Zircon-apatite method
Tongshanling	108–97 65–61	97–65	18 7.5	0.63	0.177–0.266	0.107–0.149
Weijia	158–0		0.25		0.008–0.013	
Jiuyishan	146–142	142–0	50	0.35	0.057–0.086	
Dayishan	96–80 60–0	80–60	5.6 2.3	1.0	0.087–0.130	
Baoshan	66–63		10		0.016–0.024	0.038–0.054
Qitianling	114–100 41–39	100–41	15 15	0.34	0.111–0.167	0.069–0.095
Wangxianling	172–102 86–82 59–52	102–86 82–59	1.5 5 16	0.25 0.23	0.068–0.102	
Qianlishan	146–133 100–86	133–100	6.9 10	0.61	0.139–0.208	0.800–1.114

Given the different He closure temperatures of zircon and apatite, the exhumation rate also can be calculated from the difference between the ZHe and AHe ages for a given sample based on the following equation:

$$V = (T_{Zr} - T_{Ap}) / ((t_{Zr} - t_{Ap}) * \Delta T_G)$$

where V is exhumation rate, T_{Zr} is closure temperature of zircon (180 ± 20℃), T_{Ap} is closure temperature of apatite (70 ± 20℃), t_{Zr} is He age of zircon, t_{Ap} is He age of apatite, and ΔT_G is paleogeothermal gradient (25 ± 5℃). Accordingly, exhumation rates are 0.128 ± 0.021 km/Myr for the Tongshanling pluton, 0.046 ± 0.008 km/Myr for the Baoshan porphyry, 0.082 ± 0.013 km/Myr for the Qitianling pluton, and 0.957 ± 0.157 for the Qianlishan pluton. These rates approximate the modelling curve-based exhumation rates (Table 3), except for the Qianlishan pluton (maybe caused by the less quantity of AHe ages), suggesting that the calculated exhumation rates are reliable.

Inverse modeling results indicates that the intracontinental E-SCB experienced multi-phase rapid exhumation (> 1 ℃/Ma) since the Triassic, primarily in the Middle to Late Jurassic (e.g., Wangxianling pluton: 172–102 Ma), Early Cretaceous (e.g., Jiuyishan pluton: 146–142 Ma; Qitainling pluton: 114–100 Ma), Late Cretaceous (e.g.,

Wangxianling pluton: 86–82 Ma; Dayishan pluton: 96–80 Ma), and the Cenozoic (e.g., Baoshan porphyry: 66–63 Ma, Qitianling pluton: 41–39 Ma; Wangxianling pluton: 59–52 Ma), although each pluton varies in exhumation phase quantity and timing (Figure 8a). However, a rough longitude gradient of exhumation is evident with an increase in the exhumation onset age moving westward from the Chenzhou–Linwu Fault. This spatial-temporal variation indicates that the far hinterland of E-SCB may have been an exhumation center prior to the Late Cretaceous. This is consistent with the observation that many Cretaceous extensional basins exist along the strike of the Chenzhou–Linwu Fault (Figure 2). Besides, long-term exhumation rates of these granitoids increase from the west to the east, suggesting that the eastern range seems to be affected by more long-term tectonism (Figure 8b).

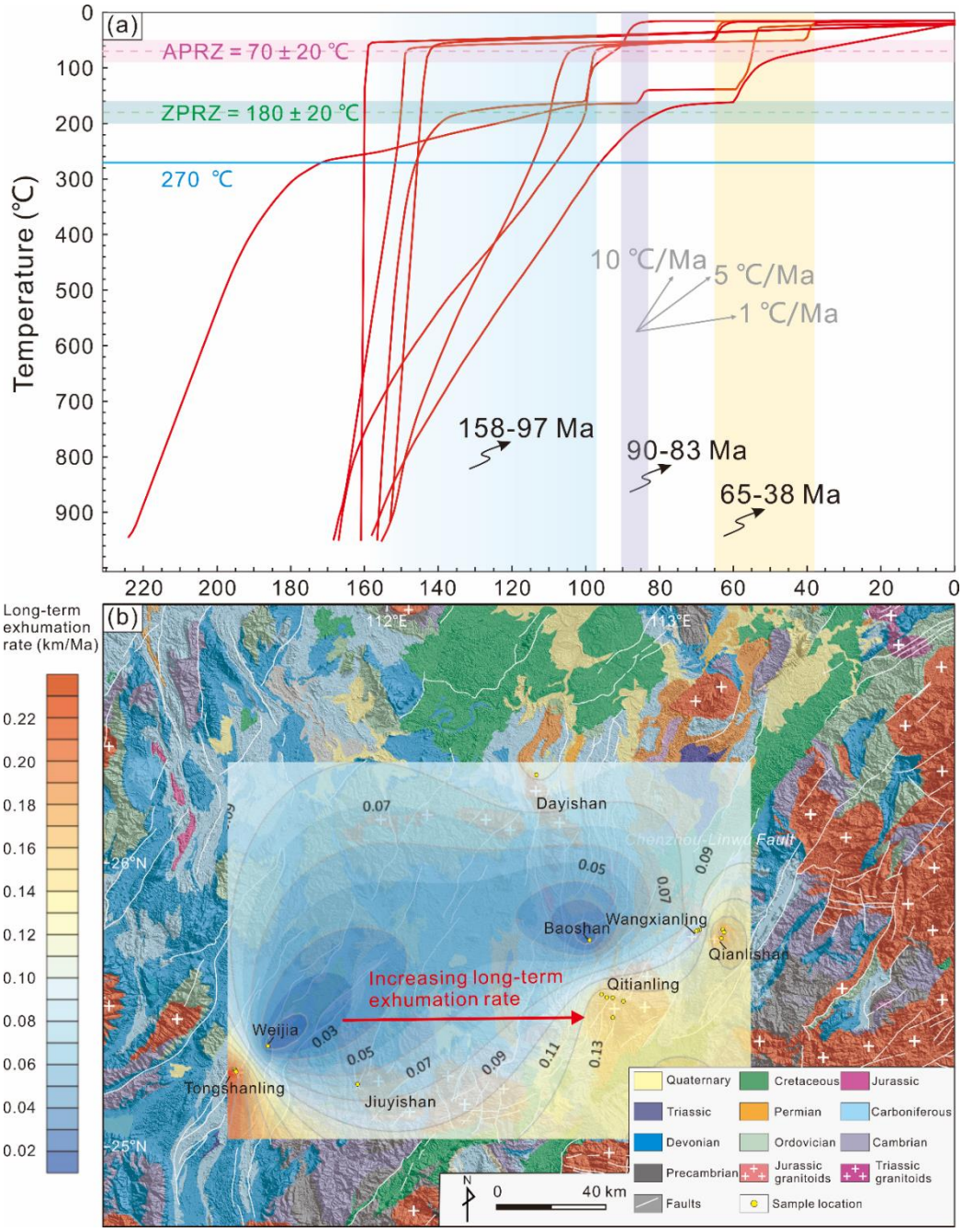

525 **Figure 8**. (a) A summary of inverse modellings of the investigated granitoids indicating
526 a three-phase exhumation in the intracontinental E-SCB; (b) Contour map showing the
527 pattern of long-term exhumation rates.

528 5.3 Implications for subduction of the Paleo-Pacific Plate

529 It has long been recognized that Mesozoic magmatism, tectonism, and
530 metallogeny in the E-SCB were primarily affected by subduction of the Paleo-Pacific

Plate, in particularly during the Middle to Late Mesozoic (Zhou et al., 2000; Li & Li, 2007; Mao et al., 2013; Li et al., 2014, Cao et al., 2021). Exhumation events in the E-SCB were a tectonic response to this subduction. Therefore, a detailed depiction of the subduction processes is crucial to better understand exhumation history of the E-SCB.

Although Mesozoic magmatism and volcanism in the E-SCB have been extensively documented (Zhou et al., 2006; Liu et al., 2020b; Li et al., 2021), a statistical study that addresses spatial and temporal variations in the Mesozoic magmatism is still lacking. Hence, we firstly calculate distances of the Mesozoic magmatic rocks away from a presumptive orogen-parallel line (mathematically expressed as $-X + Y + 97 = 0$ based on Cartesian coordinates, where X and Y are longitude and latitude in degree, respectively) (Figure 9a). K-means clustering analysis indicates that 4 age clusters are present (i.e., 256–202 Ma, 195–147 Ma, 146–117 Ma, and 116–86 Ma, Figure 9b), consistent with 4 unimodalities of the kernel density estimation (KDE) curve (Figure 9c). This indicates that the E-SCB underwent four episodes of magmatism during the Mesozoic and reveals a systematica temporal and spatial pattern: (1) in the Triassic, magmatism mostly occurred in the intracontinental E-SCB and gradually spread to the epicontinental E-SCB; (2) in the Early Jurassic, magmatism increased from the epicontinental to the intracontinental E-SCB, peaking in the Late Jurassic; (3) in the Early Cretaceous, magmatism intensified again in the intracontinental E-SCB and trended to the margin over time; and (4) massive magmatism migrated to the epicontinental E-SCB during the Late Cretaceous (Figure 9a).

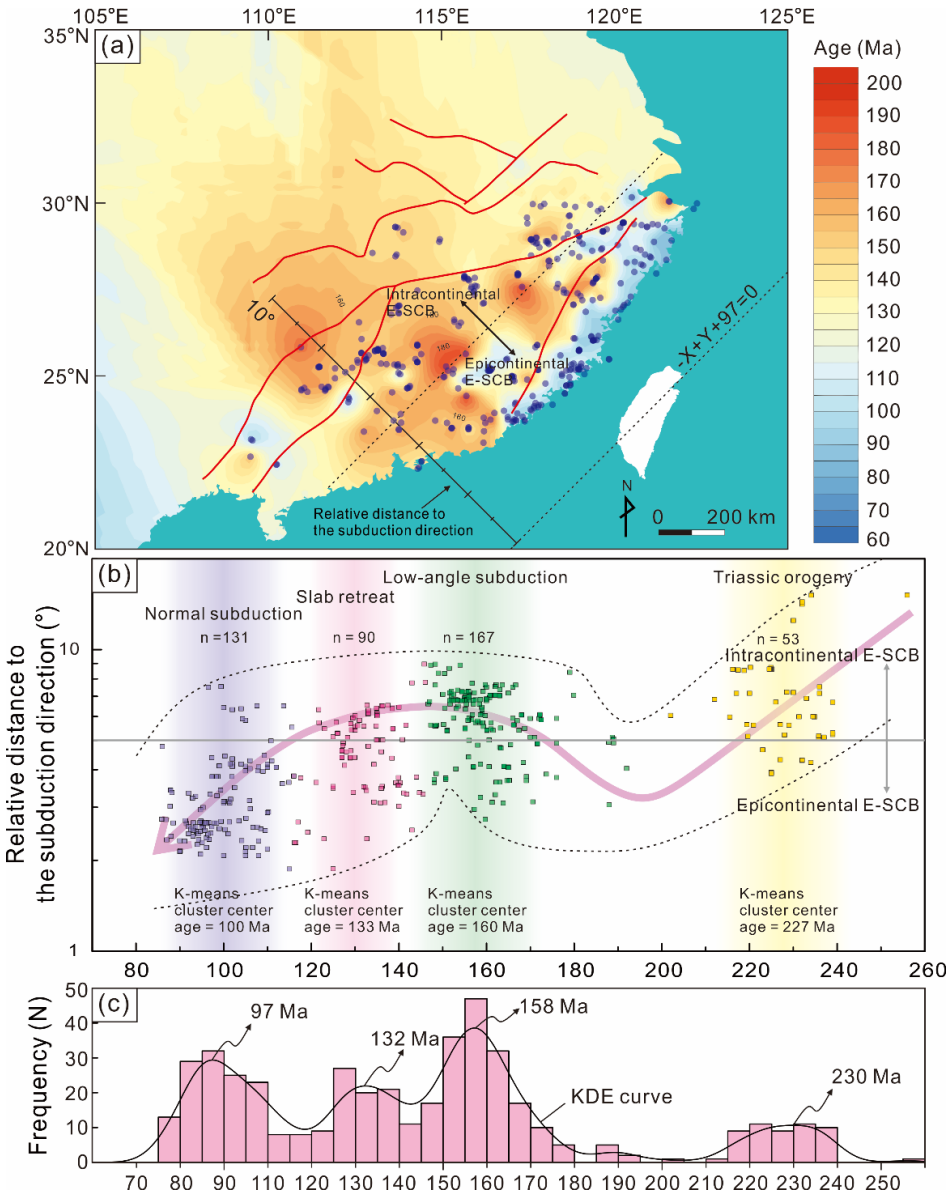

555 **Figure 9**. (a) Contour map showing the Jurassic to Cretaceous magmatism distribution
556 and age variation of the E-SCB (Data source: Liu et al., 2020b; dark blue points are
557 locations of magmatic rocks); (b) Magmatic age vs. relative distance to the subduction
558 plot showing the spatial-temporal change of the Mesozoic magmatism in the E-SCB;
559 and (c) Frequency histogram showing the age clusters of the Mesozoic magmatism in
560 the E-SCB.

561 The spatial-temporal pattern of Triassic magmatism is tectonically
562 unreconciled with northwestward subduction of the Paleo-Pacific Plate, arguing
563 against Triassic subduction onset of the Paleo-Pacific Plate for the following reasons:

(1) almost all the Triassic magmatic rocks are granitoids and no large-scale Triassic arc magmatism or magmatic rocks with subduction-related signature have been identified in the SCB, especially in the margin of the E-SCB (Shu et al., 2008; Gao et al., 2017); (2) a NE-trending A-type granitoid belt was recognized in the epicontinental SCB (e.g., Zhejiang and Fujian provinces), indicative of an extensional setting, inconsistent with the compressional setting induced by oceanic subduction (Sun et al., 2017; Xia & Xu, 2020); (3) Triassic structural patterns are characterized by WNW-trending folds and NE-striking ductile shear zones, which kinematically point to an NNE-trending (rather than NW-trending) crustal shortening (Li et al., 2017).

On the other hand, the Middle to Late Mesozoic magmatism is the most likely to be rendered by the oceanic subduction and the spatial-temporal pattern of magmatism fingerprints a multi-phase change of the subduction process, notwithstanding the subduction process needs to be further specified. In the following parts, we will discuss multi-phase subduction process from magmatic, metallogenic, geophysical, and tectonic perspectives.

The Jurassic magmatism is characterized by voluminous granitoids and sporadic mantle-derived rocks (Zhou et al., 2006; Cao et al., 2021). According to the spatial-temporal pattern of Jurassic magmatism (Figure 9b), the earliest Jurassic magmatism took place in the sub-epicontinental E-SCB and arc magmatism was handful in the epicontinental E-SCB (Zhou et al., 2000; Cao et a., 2021). The location and petrogenesis of the Jurassic magmatism imply a low-angle subduction model. This is because of a slow increase of heat and pressure during the low-angle subduction that prevents the slab from large-scale partial melting and dehydration, as a result of which a long subduction distance is required for generating magmatism. With the ongoing low-angle subduction process, slab reached the intracontinental E-SCB and broke off due to the gravitational instability in the Late Jurassic. The foundering of broke-off slab caused an upwelling of asthenosphere and consequent lithospheric extension. In response, A-type granitoids, as a high-temperature remelting

593 product, were extensively produced during this stage and accompanied with intensive
594 world-class W-Sn polymetallic metallogeny.

595 This low-angle subduction model also can well explain the diversity of
596 Jurassic magmatism and related mineralization. Specifically, recent studies on
597 Jurassic magmatism and related metallogeny recognized an underlying porphyry Cu
598 metallogenic belt (e.g., Dexing and Yinshan deposits) in the epicontinental to
599 sub-epicontinental E-SCB, with a gradual change of metallogenic age from 178 to
600 155 Ma (Mao et al., 2013, 2021). Porphyry Cu deposits, as the sign of oceanic
601 subduction, has been well documented to mostly occur during a flat-slab or low-angle
602 subduction process (Sillitoe et al., 2010). Hence, the presence of porphyry Cu
603 metallogenic belt in the margin of E-SCB favors a low-angle subduction, similar to
604 the porphyry Cu provinces of the Andes (Sillitoe & Perelló, 2005; Sillitoe et al., 2010).
605 In contrast, W–Sn deposits related to A-type granitoids have a later mineralization
606 time approximately of 160–150 Ma and intensively developed in the intracontinental
607 E-SCB, especially for the Sn mineralization. Given that an intensive heat supply or
608 extensional setting is required for generating A-type magmatism (Clemens et al.,
609 1986), such a metallogenic sequence illustrates that the slab may undergo break-off in
610 the intracontinental E-SCB as the slab advanced. In addition, Yuan et al. (2019)
611 proposed that Sn mineralization was dominated in the far intracontinental E-SCB and
612 it was determined by an extremely high melting temperature and the addition of
613 mantle melts to the magma chamber. This indicates that the far intracontinental
614 E-SCB (the west of Chenzhou–Linwu Fault) is likely the center of slab break-off,
615 consistent with the westward aging trend of exhumation timing in the intracontinental
616 E-SCB. Other geological evidence also records a difference between the
617 intracontinental and epicontinental E-SCB, such as the differentiated magna sources
618 of Jurassic mafic rocks between these two areas (OIB-dominated vs. EM2) (Wang et
619 al., 2003), contrasting metasomatized lithospheric mantle beneath the intracontinental
620 and sub-epicontinental E-SCB (altered by slab-derived melts and fluids, respectively)
621 (Liu et al., 2020a), and significant lithospheric differences between western and

622 eastern sides of the 114° longitude (Yin et al., 2021). These lines of evidence further
623 suggests that the oceanic subduction and slab break-off occurred in the Jurassic.

624 Most Cretaceous magmatic rocks of the E-SCB are volcanic arc rocks (e.g.,
625 rhyolite, dacites, andesites, and basalts, Li et al., 2014; Cao et al., 2021). Furthermore,
626 the notable NE-striking extensional basins and magmatic belts indicate a coeval NW–
627 SE crustal extension in the E-SCB, related to an ongoing northwestward subduction
628 of the Paleo-Pacific Plate during the Cretaceous. In contrast to the Jurassic
629 magmatism, the Cretaceous magmatism was shifted from the intracontinental to the
630 sub-margin and the margin of E-SCB in the Early and Late Cretaceous, respectively
631 (Figure 9b, Cao et al., 2021). Furthermore, Cretaceous mafic magmatism is more
632 intensive than that of the Jurassic and high-angle oceanic subduction favors extensive
633 dehydration of the slab and the addition of slab-derived fluid/melt contributes greatly
634 to the partial melting of mantle (Wang et al., 2010; Meng et al., 2012). This
635 spatial-temporal pattern of Cretaceous magmatism decodes that the Jurassic low-angle
636 subduction had been converted into a normal subduction and retreated as a
637 consequence of the tugging of foundered slab. Meanwhile, Cretaceous mineralization
638 was lesser in the intracontinental E-SCB, further suggesting a progressive retreat of
639 the slab (Mao et al., 2013).

640 In summary, the multi-perspective geological evidences, together with
641 spatial-temporal pattern of the Mesozoic magmatism, outline a trilogy of subduction
642 process of the Paleo-Pacific Plate: (1) in the Early Jurassic, the Paleo-Pacific Plate
643 initiated a low-angle subduction (Figure 10a) and reached the intracontinental SCB
644 probably during the Middle Jurassic, with slab break-off occurring in the Late Jurassic
645 (Figure 10b); (2) in the Early Cretaceous, the oceanic subduction gradually increased
646 the subduction angle as pulled by the foundering slab (Figure 10c); and (3) in the Late
647 Cretaceous, the slab retreated to the epicontinental E-SCB, changed into a normal
648 subduction, and generated voluminous arc plutonism and volcanism (Figure 10d).

649

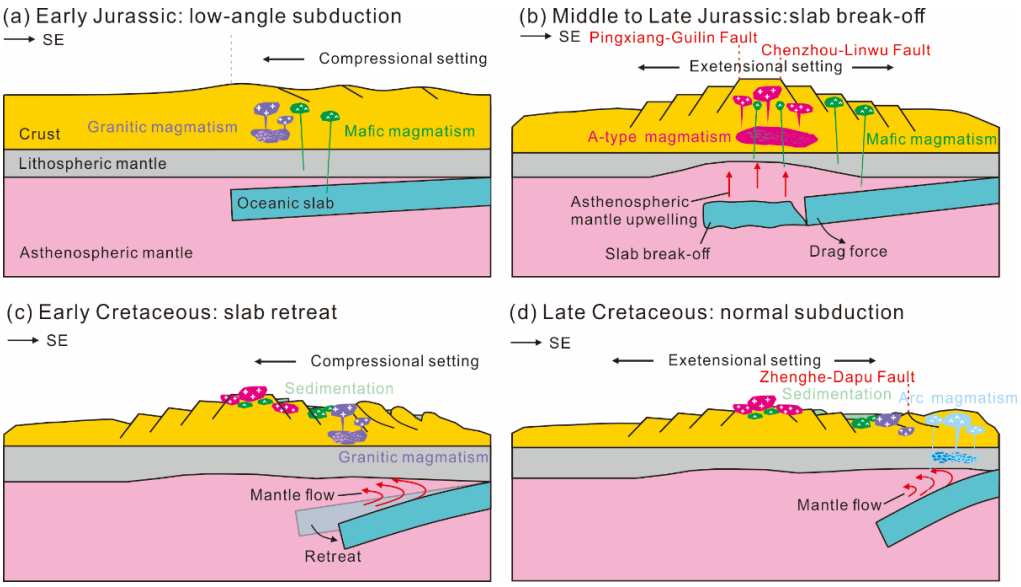

Figure 10. A cartoon illustrating the tectonic evolution of the E-SCB: (a) Early Jurassic low-angle subduction; (b) Middle to late Jurassic slab break-off and foundering; (c) Early Cretaceous slab retreat with angle changing; and (d) Late Cretaceous normal subduction.

5.4 Structural analysis of the E-SCB

Tectonic stress features of major Jurassic to Cretaceous basins are synthesized to reveal the tectonic evolution of the E-SCB and to further understand the exhumation history of the E-SCB (Zhou et al., 2006; Wu et al., 2013). Quantitative stress tensor inversion is conducted via the classic inverse method (Yamaji, 2000).

The stress distribution of Early Jurassic basins is characterized by sub-horizontal SE-trending σ_1, ENE-trending σ_2, and vertical σ_3 (Figure 11a). In addition, most Early to Middle Jurassic folds in the E-SCB have NE/NNE-trending axes, together with the stress tensor inversion results, indicative of a compressional stress mode (Li et al., 2021). This tectonic pattern implies that the E-SCB may have been compressed by the Paleo-Pacific Plate assembly in the Early to Middle Jurassic (Wang et al., 2013; Zhong et al., 2017).

In the Late Jurassic, the overall stress field applying to the E-SCB were significantly changed, the direction of the maximum principal stress axis had changed

668 from sub-horizontal to vertical in the Late Jurassic according to the stress tensor
669 inversion results (Figure 11b). This means that the stress field mode has changed from
670 compression to extension. Since the Late Jurassic basins are mostly distributed in the
671 epicontinental E-SCB, this stress orientation reversal may be caused by the deep
672 magmatic activity caused by subduction. (i.e., extension of the intracontinental E-SCB,
673 Sun et al., 2006; Li et al., 2021).

674 The Early Cretaceous NW–SE transpression was documented by conjugated
675 NW-striking dextral and NE-striking sinistral faults in the Huichang basin (Figure 11c)
676 and syntectonic basins along the epicontinental E-SCB (Figures 11d–g) (Morinaga &
677 Liu, 2004; Lin et al., 2015). The stress distributions are characterized by a
678 sub-horizontal NW-trending σ_1, sub-vertical σ_2, and sub-horizontal NE-trending σ_3,
679 indicating another strike slip event in the E-SCB (Li et al., 2014). This strike slip
680 event is widely believed to be related to the compression of the Paleo-Pacific Plate in
681 the Early Cretaceous, although the slip vector data related to this transpression are
682 sparse in the inland, the transpressional event is, none the less, thought to have
683 resulted in significant deformation, including regional crustal shortening and tectonic
684 inversion of South China (Lapierre et al., 1997).

685 The Late Cretaceous extension was accommodated by reactivation of
686 pre-existing faults. As this extension involved the Lower to Upper Cretaceous strata
687 (Li et al., 2014), the WNW–ESE extension is likely to occur during or after the Early
688 Cretaceous. This extension may produce intensive volcanism in the epicontinental
689 E-SCB and the duration (107–86 Ma) of magmatism further constrains the timing of
690 this extension (Wu et al., 2012). The WNW–ESE extension gave rise to N-S- to
691 NNE-striking normal faults with WNW-trending striation in the Ji'an, Guangchang,
692 Yongkang, and the epicontinental basins (Figures 11h–l), with stress distributions of
693 vertical σ_1, sub-horizontal NE-trending σ_2, and WNW-trending σ_3.

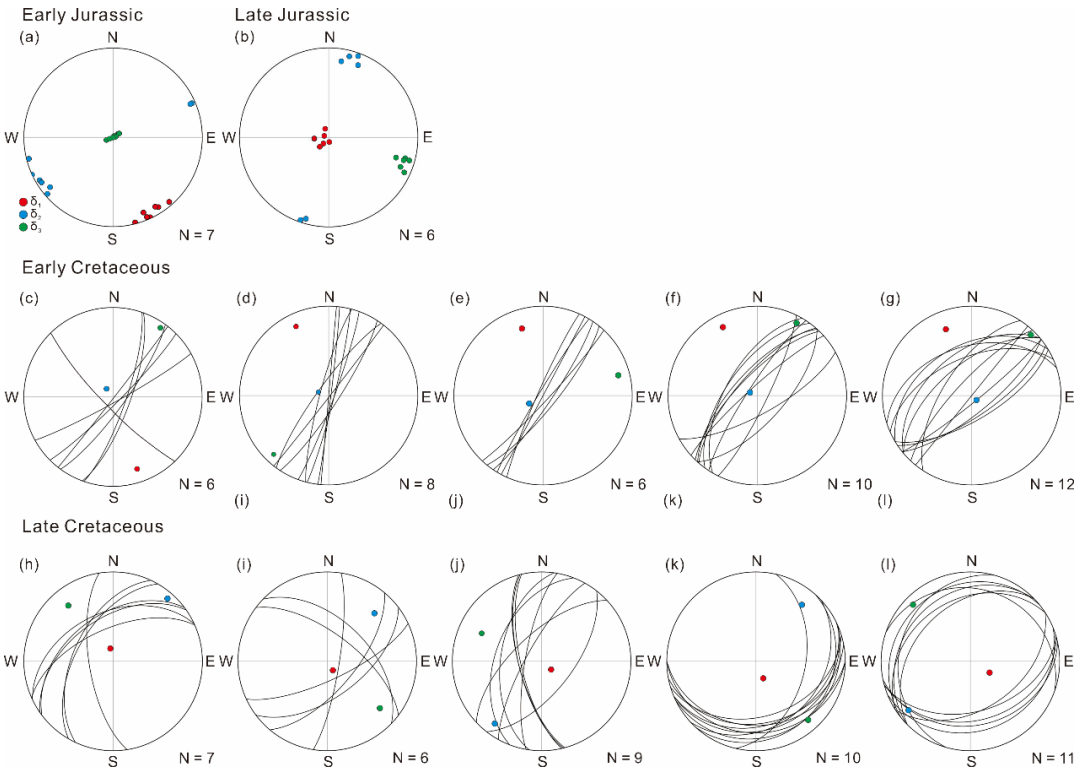

Figure 11. Tectonic stress fields of (a) Early Jurassic E-SCB; (b) Late Jurassic E-SCB; (c) Early Cretaceous Huichang basin; (d–g) Early Cretaceous basins in the epicontinental E-SCB; (h) Late Cretaceous Ji'an Basin; (i) Late Cretaceous Guangchang Basin; (j) Late Cretaceous Yongkang Basin; and (k–l) Late Cretaceous basins in the epicontinental E-SCB. (Data source: Li et al., 2014, 2021). All projections are lower sphere and equal area.

5.5 Multiple exhumation and its insights into evolution of the E-SCB

Exhumation history of the E-SCB remains enigmatic due to a handful of low temperature thermochronological studies. Until recently, low temperature thermochronological studies just sprang up and revealed a large variation of (U-Th)/He and fission track ages in the E-SCB (e.g., Su et al., 2017; Tao et al., 2017, 2019; Wang et al., 2020; Sun et al., 2021). Previously published ZHe and AHe ages are locally reported and range from 152–24 Ma (n = 82) and 69–23 Ma (n = 30), respectively (Table S4). In contrast, ZFT and AFT ages have been extensively

709 presented with onset time spans of 144–70 Ma (n = 71) and 93–24 Ma (n = 167),
710 respectively (Table S4).

711 However, these studies failed to give consistent interpretations to exhumation
712 history of the E-SCB, in particularly since the Early Cretaceous. For example, Su et al.
713 (2017) investigated Mesozoic rocks in both sides of the Chenzhou–Linwu Fault
714 (intracontinental E-SCB) and suggested that the exhumation initiated from 45–35 Ma
715 and 36–23 Ma, respectively. Sun et al. (2021) indicated a two-stage exhumation of the
716 Changjiang uranium ore field (intracontinental E-SCB) during ~80–60 Ma and ~40–0
717 Ma. Ding et al. (2019) pointed out one exhumation event from ~150 Ma to 110 Ma
718 and another one between ~100–80 Ma took place in the epicontinental E-SCB. Tao et
719 al. (2017) indicated ~140–70 Ma and ~53–36 Ma exhumation events of the
720 epicontinental E-SCB. Wang et al. (2020) identified two major exhumation events of
721 the E-SCB occurring in the Cretaceous (~125–80 Ma) and Late Cretaceous–
722 Paleogene (~80–25 Ma) based on regional AFT analyses. The diversified
723 interpretations of exhumation history are likely to result from a complicated Mesozoic
724 to Cenozoic tectonism. On the other hand, the irreconcilable interpretations may be
725 caused by using multi-interpretable and low-reproducible HeFTy program which were
726 employed by most studies.

727 In comparison, our mutually validated thermochronological modelling results
728 register a more sophisticated three-phase exhumation history of the intracontinental
729 SCB, which commenced in the Late Jurassic–Early Cretaceous, renewed in the Late
730 Cretaceous, and dissipated over the Paleogene, regardless of localized difference
731 (Figure 8a). The inverse modelling results attest a previous speculation that the
732 E-SCB experienced multiple exhumation since the Triassic (Li et al., 2014; Chu et al.,
733 2019), although the onset time is variable. However, a rapid post-Paleogene (< 23 Ma)
734 exhumation is not observed in most samples, suggesting that post-Paleogene
735 tectonism was more limited and weaker within the intracontinental E-SCB than
736 previously suggested (Su et al., 2017; Tao et al., 2017, 2019; Sun et al., 2021). To
737 avoid a bias of a local scope study, thermochronological age mapping is employed to

constrain regional exhumation history of the E-SCB. A synthesis of ZHe/ZFT dates (Figures 12a–b) shows that the intracontinental E-SCB was exhumated to the ZPRZ (5–10 km under the surface) prior to the epicontinental E-SCB in the Early Cretaceous. In contrast, regional AFT/AHe data demonstrates a sketchy ageing trend (from 20 Ma to 90 Ma) towards the southeastern E-SCB (Figures 12c–d). This indicates that exhumation activity in the intracontinental E-SCB weakened progressively and the epicontinental E-SCB underwent much significant exhumation of 1–5 km during the Late Cretaceous–Paleogene, probably due to the slab retreat. The southeastward propagation of exhumation center is consistent with the above refined subduction process, indicating that intensity of exhumation in the E-SCB was correlated with slab advance and retreat. Hence, the Cretaceous slab retreat is hypothesized to be a major cause responsible for regional exhumation event of the E-SCB.

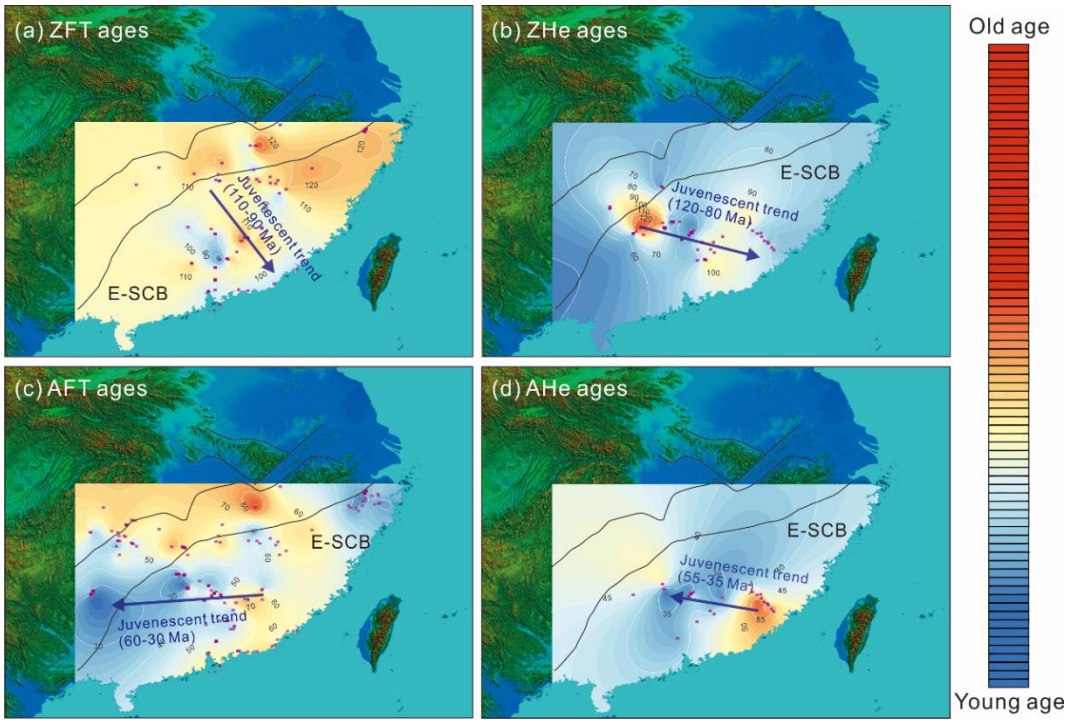

Figure 12. Contour maps of (a) post-Triassic ZFT ages; (b) post-Triassic AFT ages; (c) post-Triassic ZHe ages; and (d) post-Triassic AHe ages in the E-SCB. (Data source: Yi

et al., 2009; Tang et al., 2014; Wang et al., 2015, 2018, 2020a, b; Li et al., 2016b; Li & Zou, 2017; Su et al., 2017; Tao et al., 2017, 2019; Ding et al., 2019; Qiu et al., 2019; Chu et al., 2020; Sun et al., 2021)

Mesozoic exhumation history of the E-SCB also sheds new light on the interplay of tectonism, topography and climatology. The present-day E-SCB has been in an East Asian monsoon climate characterized by high temperature, humid, and monsoon-drenched (Garzanti et al., 2021). This climate was suggested to be prevalent associated with the uplift of the Tibetan Plateau from the Middle–Late Eocene (Xie et al., 2019). In comparison, Cretaceous basins of the E-SCB are identified as inland faulted basins, in which thick Late Cretaceous to Early Paleogene sedimentary red beds and evaporites mirror an arid desert climate (Jiao et al., 2020; Xie et al., 2020). The formation of these arid basins may be associated with the Late Cretaceous rapid exhumation of the epicontinental E-SCB. Based on the thermochronological synthesis, apatite helium and fission track ages of the E-SCB roughly show an ageing propagation from the intracontinental to the epicontinental E-SCB, suggesting that the epicontinental E-SCB was foremost exhumated to the surface and formed a paleo high-relief margin. Sedimentary study elucidates different sedimentary provenances of Triassic granitoids and Jurassic to Cretaceous magmatic (120–90 Ma) rocks for the Lower and Upper Cretaceous sandstones of the E-SCB, respectively, consistent with a significant exhumation of the Jurassic to Early Cretaceous magmatic rocks during the Late Cretaceous to Paleogene (Yan et al., 2011). Accordingly, the paleo-river-network has been recognized to flow westwards from the epicontinental E-SCB and debouch in dry inland lakes (Shu et al., 2009). In addition, Li et al. (2014) found that Late Cretaceous sedimentary formations of the epicontinental E-SCB are thicker than those of the intracontinental E-SCB, indicating that the epicontinental E-SCB was significantly eroded and basins in this region accumulated massive sediments. This exhumation seems to initiate from the Late Cretaceous as indicated by different sediment provenances and widespread unconformity of Upper and Lower Cretaceous sedimentary rocks (Li et al., 2014). These evidences indicate an existence of mountain

belt in the epicontinental E-SCB during the Late Cretaceous to the Early Paleogene. The towering mountains along the epicontinental E-SCB acted as a natural barrier that prevented a transport of oceanic water vapor to the hinterland E-SCB. Thus, this topographical setting created a rain–shadow effect that intensified the aridification and formed extensive arid basins in the intracontinental SCB until to the uplift of the Tibetan Plateau, similar to role of the Great Dividing Range in controlling extensive deserts in the central Australia.

6 Conclusions

1. ZHe and AHe ages suggest the intracontinental SCB experienced multiple exhumation from the Late Jurassic with variable onset timing and the far hinterland E-SCB may be an exhumation center at least in the Early Cretaceous (the west of the Chenzhou–Linwu Fault).

2. A synthesis from multiple geological perspectives indicates that subduction of the Paleo-Pacific Plate was initiated in the Early Jurassic, and that the plate underwent slab break-off and foundering in the Late Jurassic, with subduction gradually retreating to the epicontinental E-SCB and being transformed to a normal sense during the Cretaceous.

3. A regional map of low-temperature thermochronological data favors subduction of the Paleo-Pacific Plate as a major geodynamic trigger for post-Jurassic exhumation of the E-SCB.

4. A refined model based on low-temperature thermochronology is proposed to interpret the exhumation, topographic, and climatical evolution of the E-SCB.

Acknowledgements

This work was financed by National Key Research and Development Plan (Grant No. 2018YFC0603902). Mr. Jinghua Wu was funded by the China Scholarship Council (No. 202006370297) during his visiting and study at the Kyushu University, Japan, which is greatly acknowledged. We would like to thank Dr. Huashan Sun for

helpful discussions. We acknowledge the help of Dr. Martin Danišík with (U-Th)/He analyses at Low Temperature Thermochronology Facility of the John de Laeter Centre, Curtin University. Dr. Martin Danišík was supported by Australian Scientific Instruments Pty Ltd., Australian Research Council (ARC) Discovery funding scheme (DP160102427) and a Curtin Research Fellowship (CRF170135). We are grateful to Prof. Noreen J. Evans for her constructive comments and great help to improve this paper. The supplementary data of this paper can be freely accessed on the Mendeley Data at https://data.mendeley.com/drafts/vpgcdwn569 (DOI: 10.17632/vpgcdwn569.1).

References

Ault, A.K., & Flowers, R.M. (2012). Is apatite U–Th zonation information necessary for accurate interpretation of apatite (U–Th)/He thermochronometry data? *Geochimica et Cosmochimica Acta*, 79, 60–78. https://doi.org/10.1016/j.gca.2011.11.037

Barbarand, J., Carter, A., Wood, I., & Hurford, T. (2003). Compositional and structural control of fission-track annealing in apatite. *Chemical Geology*, 198, 107–137. https://doi.org/10.1016/S0009-2541(02)00424-2

Brady, R.J. (2002). Very high slip rates on continental extensional faults: new evidence from (U–Th)/He thermochronometry of the Buckskin Mountains, Arizona. *Earth and Planetary Science Letters*, 197, 95–104. https://doi.org/10.1016/002689700417574

Brown, R.W., Beucher, R., Roper, S., Persano, C., Stuart, F., & Fitzgerald, P. (2013). Natural age dispersion arising from the analysis of broken crystals. Part I: Theoretical basis and implications for the apatite (U–Th)/He thermochronometer. *Geochimica et Cosmochimica Acta*, 122, 478–497. https://doi.org/10.1016/j.gca.2013.05.041

Cao, X., Flament, N., Li, S., & Müller, R.D. (2021). Spatio-temporal evolution and dynamic origin of Jurassic-Cretaceous magmatism in the South China Block. *Earth-Science Reviews*, 217. https://doi.org/10.1016/j.earscirev.2021.103605

839 Cawood, P.A., Zhao, G., Yao, J., Wang, W., Xu, Y., & Wang, Y. (2018).
840 Reconstructing south China in Phanerozoic and Precambrian supercontinents.
841 *Earth-Science Reviews*, 186, 173–194.
842 https://doi.org/10.1016/j.earscirev.2017.06.001
843 Chen, J., Qingfei, W., Qiao, L., Liu, X., & Zhang, Q. (2020). Cretaceous exhumation
844 history of the southwestern South China Block: Constraints from fission-track
845 thermochronology. *Geological Journal*, 55. https://doi.org/10.1002/gj.3837
846 Cherniak, D.J., & Watson, E.B. (2001). Pb diffusion in zircon. *Chemical Geology*, 172,
847 5–24. https://doi.org/10.1016/S0009-2541(00)00233-3
848 Chu, Y., Faure, M., Zhenhua, X., Ji, W., & Feng, Z. (2019). Cretaceous episodic
849 extension in the South China Block, East Asia: evidence from the Yuechengling
850 Massif of Central South China. *Tectonics*, 38, 3675–3702.
851 https://doi.org/10.1029/2019TC005516
852 Chu, Y., Lin, W., Faure, M., Allen, M.B., & Feng, Z. (2020). Cretaceous exhumation
853 of the Triassic intracontinental Xuefengshan Belt: Delayed unroofing of an
854 orogenic plateau across the South China Block? *Tectonophysics*, 793.
855 https://doi.org/10.1016/j.tecto.2020.228592
856 Clark, M.K., Farley, K.A., Zheng, D., Wang, Z., & Duvall, A.R. (2010). Early
857 Cenozoic faulting of the northern Tibetan Plateau margin from apatite (U–
858 Th)/He ages. *Earth and Planetary Science Letters*, 296, 78–88.
859 https://doi.org/10.1016/j.epsl.2010.04.051
860 Clemens, J., Holloway, J.R., & White, A.J.R. (1986). Origin of an A-type granite:
861 experimental constraints. *American Mineralogist*, 71, 317–324.
862 Crowley, K.., Cameron, M., Schaefer, R. (1991). Experimental studies of annealing of
863 etched fission tracks in fluorapatite. *Geochimica et Cosmochimica Acta*, 55,
864 1449–1465. https://doi.org/10.1016/0016-7037(91)90320-5
865 Deng, X.D., Li, J.W., & Shuster, D.L. (2017). Late Mio-Pliocene chemical weathering
866 of the Yulong porphyry Cu deposit in the eastern Tibetan Plateau constrained by
867 goethite (U–Th)/He dating: Implication for Asian summer monsoon. *Earth and*

Planetary Science Letters, 472, 289–298. https://doi.org/10.1016/j.epsl.2017.04.043

Ding, R., Min, K., & Zou, H. (2019). Inversion of topographic evolution using low-T thermal history: A case study from coastal mountain system in Southeastern China. *Gondwana Research*, 67, 21–32. https://doi.org/10.1016/j.gr.2018.09.009

Evans, N., Byrne, J., Keegan, J., & Dotter, L. (2005). Determination of Uranium and Thorium in Zircon, Apatite, and Fluorite: Application to Laser (U-Th)/He Thermochronology. *Journal of Analytical Chemistry*, 60, 1159–1165. https://doi.org/10.1007/s10809-005-0260-1

Faure, M., Lin, W., Chu, Y., & Lepvrier, C. (2016). Triassic *Tectonics*, of the southern margin of the South China Block. *Comptes Rendus Geoscience*, 348(1), 5–14. https://doi.org/10.1016/j.crte.2015.06.012

Fitzgerald, P.G., Baldwin, S.L., Webb, L.E., & O'Sullivan, P.B. (2006). Interpretation of (U–Th)/He single grain ages from slowly cooled crustal terranes: A case study from the Transantarctic Mountains of southern Victoria Land. *Chemical Geology*, 225, 91–120. https://doi.org/10.1016/j.chemgeo.2005.09.001

Flowers, R., Shuster, D., Wernicke, B., & Farley, K. (2007). Radiation damage control on apatite (U-Th)/He dates from the Grand Canyon region, Colorado Plateau. *Geology*, 35. https://doi.org/10.1130/G23471A.1

Gao, P., Zheng, Y.F., & Zhao, Z.F. (2017). Triassic granites in South China: A geochemical perspective on their characteristics, petrogenesis, and tectonic significance. *Earth-Science Reviews*, 173, 266–294. https://doi.org/10.1016/j.earscirev.2017.07.016

Gallagher, K. (2012). Transdimensional Inverse Thermal History Modelling for Quantitative Thermochronology. *Journal of Geophysical Research: Solid Earth*, 117. https://doi.org/10.1029/2011JB008825

Garzanti, E., He, J., Barbarano, M., Resentini, A., Li, C., Yang, L., Yang, S., & Wang, H., (2021). Provenance versus weathering control on sediment composition in tropical monsoonal climate (South China) - 2. Sand petrology and heavy

minerals. *Chemical Geology*, 564. https://doi.org/10.1016/j.chemgeo.2020.119997

Gautheron, C., Tassan-Got, L., Barbarand, J., & Pagel, M. (2009). Effect of alpha-damage annealing on apatite (U–Th)/He thermochronology. *Chemical Geology*, 266, 157–170. https://doi.org/10.1016/j.chemgeo.2009.06.001

Glotzbach, C., Van der Beek, P.A., & Spiegel, C. (2011). Episodic exhumation and relief growth in the Mont Blanc massif, Western Alps from numerical modelling of thermochronology data. *Earth and Planetary Science Letters*, 304, 417–430. https://doi.org/10.1016/j.epsl.2011.02.020

Guenthner, W., Reiners, P., Ketcham, R., Nasdala, L., & Giester, G. (2013). Helium diffusion in natural zircon: Radiation damage, anisotropy, and the interpretation of zircon (U-Th)/He thermochronology. *American Journal of Science*, 313. https://doi.org/10.2475/03.2013.01

Guillaume, B., Gautheron, C., Simon-Labric, T., Martinod, J., Roddaz, M., & Douville, E. (2013). Dynamic topography control on Patagonian relief evolution as inferred from low temperature thermochronology. *Earth and Planetary Science Letters*, 364, 157–167. https://doi.org/10.1016/j.epsl.2012.12.036

Jacob, J.B., & Moyen, J.F., (2021). Encyclopedia of Geology (Second Edition). In: Alderton, D., Elias, S.A.B.T.E. of G. (Second E. (Eds.), *Granite and Related Rocks* (pp. 170–183). Oxford: Academic Press.

Jiao, H., Wu, C., Rodríguez-López, J.P., Sun, X., & Yi, H., (2020). Late Cretaceous plateau deserts in the South China Block, and Quaternary analogues; sedimentology, dune reconstruction and wind-water interactions. *Marine and Petroleum Geology*, 120. https://doi.org/10.1016/j.marpetgeo.2020.104504

Jiang, W.C., Li, H., Turner, S., Zhu, D.P., & Wang, C., (2020). Timing and origin of multi-stage magmatism and related W–Mo–Pb–Zn–Fe–Cu mineralization in the Huangshaping deposit, South China: An integrated zircon study. *Chemical Geology*, 552. https://doi.org/10.1016/j.chemgeo.2020.119782

Jiang, Y.H., Jiang, S.Y., Dai, B.Z., Liao, S.Y., Zhao, K.D., & Ling, H.F. (2009).

Middle to late Jurassic felsic and mafic magmatism in southern Hunan province, southeast China: Implications for a continental arc to rifting. *Lithos*, 107, 185–204. https://doi.org/10.1016/j.lithos.2008.10.006

Jiang, Y.H., Wang, G.C., Liu, Z., Ni, C.Y., Long, Q., & Zhang, Q. (2015). Repeated slab advance–retreat of the Paleo-Pacific Plate underneath SE China. *International Geology Review*, 57 (4), 472–491. https://doi.org/10.1080/00206814.2015.1017775

Käßner, A., Stanek, K.P., & Lapp, M., (2020). Post-Variscan tectonic and landscape evolution of the Elbe Fault Zone and the Lusatian Block based on apatite fission-track data and geomorphologic constraints. *Geomorphology*, 355. https://doi.org/10.1016/j.geomorph.2019.106860

Ketcham, R. (2005). Forward and inverse Modeling of low-temperature thermochronometry data. *Reviews in Mineralogy and Geochemistry*, 58(1), 275–314. https://doi.org/10.2138/rmg.2005.58.11

Kong, H., Li, H., Wu, Q.H., Xi, X.S., Dick, J.M., & GaboRatio, J.A.S. (2018). Co-development of Jurassic I-type and A-type granites in southern Hunan, South China: Dual control by plate subduction and intraplate mantle upwelling. *Geochemistry*, 78, 500–520. https://doi.org/10.1016/j.chemer.2018.08.002

Lapierre, H., Jahn, B.M., Charvet, J., & Yu, Y.W. (1997). Mesozoic felsic arc magmatism and continental olivine tholeiites in Zhejiang Province and their relationship with the tectonic activity in southeastern China. *Tectonophysics*, 274, 321–338. https://doi.org/10.1016/S0040-1951(97)00009-7

Li, C., Wang, Z., Lü, Q., Tan, Y., Li, L., & Tao, T. (2021). Mesozoic tectonic evolution of the eastern South China Block: A review on the synthesis of the regional deformation and magmatism. *Ore Geology Reviews*, 131. https://doi.org/10.1016/j.oregeorev.2021.104028

Li, H., Wu, J.H., Evans, N.J., Jiang, W.C., & Zhou, Z.K. (2018). Zircon geochronology and geochemistry of the Xianghualing A-type granitic rocks: Insights into multi-stage Sn-polymetallic mineralization in South China. *Lithos*,

312–313, 1–20. https://doi.org/10.1016/j.lithos.2018.05.001

Li, J., Zhang, Y., Dong, S., & Johnston, S.T. (2014). Cretaceous tectonic evolution of South China: A preliminary synthesis. *Earth-Science Reviews*, 134, 98–136. https://doi.org/10.1016/j.earscirev.2014.03.008

Li, J., Shi, W., Zhang, Y., Dong, S., & Ma, Z. (2016b). Thermal evolution of the Hengshan extensional dome in central South China and its tectonic implications: new insights into low-angle detachment formation. *Gondwana Research*, 35, 425–441. https://doi.org/10.1016/j.gr.2015.06.008

Li, J., Zhang, Y., Zhao G., Johnston, S., Dong, S., Koppers, A., Miggins, D., Sun, H., Wang, W., & Xin. Y. (2017). New insights into Phanerozoic Tectonics of South China: Early Paleozoic sinistral and Triassic dextral transpression in the east Wuyishan and Chencai domains, NE Cathaysia. *Tectonics*, 36. https://doi.org/10.1002/2016TC004461

Li, X., & Zou, H. (2017). Late Cretaceous-Cenozoic exhumation of the southeastern margin of Coastal Mountains, SE China, revealed by fission-track thermochronology: Implications for the topographic evolution. *Solid Earth Sciences*, 2, 79–88. https://doi.org/10.1016/j.sesci.2017.02.001

Li, Y., Dong, S., Zhang, Y., Li, J., Su, J., & Han, B. (2016a). Episodic Mesozoic constructional events of central South China: constraints from lines of evidence of superimposed folds, fault kinematic analysis, and magma geochronology. *International Geology Review*, 58, 1076–1107. https://doi.org/10.1080/00206814.2016.1146999

Li, Z.X., & Li, X.H. (2007). Formation of the 1300-km-wide intracontinental orogen and postorogenic magmatic province in Mesozoic south China: a flat-slab subduction model. *Geology*, 35 (2), 179–182. https://doi.org/10.1130/G23193A.1

Lin, W., Ji, W., Faure, M., Wu, L., Li, Q., Shi, Y., Scharer, U., Wang, F., & Wang, Q. (2015). Early Cretaceous extensional reworking of the Triassic HP–UHP metamorphic orogen in Eastern China. *Tectonophysics*, 662, 256–270. https://doi.org/10.1016/j.tecto.2015.05.028

Liu, B., Wu, J.H., Li, H., Wu, Q.H., Evans, N., Kong, H., & Xi, X.S., (2020a). Geochronology, geochemistry and petrogenesis of the Dengfuxian lamprophyres: Implications for the early Cretaceous tectonic evolution of the South China Block. *Geochemistry*, 80. https://doi.org/10.1016/j.chemer.2020.125598

Liu, J.X., Wang, S., Wang, X.L., Du, D.H., Xing, G.F., Fu, J.M., Chen, X., & Sun, Z.M., (2020b). Refining the spatio-temporal distributions of Mesozoic granitoids and volcanic rocks in SE China. *Journal of Asian Earth Sciences*, 201. https://doi.org/10.1016/j.jseaes.2020.104503

Liu, Y., Lai, J.Q., Xiao, W.Z., Jeffrey, M.D., Du, R.J., Li, S.L., Liu, C.Y., Wen, C.H., & Yu, X.H. (2019). Petrogenesis and mineralization significance of two-stage A-type granites in Jiuyishan, South China: Constraints from whole-rock geochemistry, mineral composition and zircon U-Pb-Hf isotopes. *Acta Geologica Sinica (English Edition)*, 93 (4), 874–900. https://doi.org/10.1111/1755-6724.13864

Mao, J.W., Cheng Y.B., Maohong, C., & Pirajno, F. (2013). Major types and time–space distribution of Mesozoic ore deposits in South China and their geodynamic settings. *Mineralium Deposita*, 48, 267–294. https://doi.org/10.1007/s00126-012-0446-z

Mao, J.W, Zheng, W., Xie, G., Lehmann, B., & Goldfarb, R., (2021). Recognition of a Middle–Late Jurassic arc-related porphyry copper belt along the southeast China coast: Geological characteristics and metallogenic implications. *Geology*, 49. https://doi.org/10.1130/G48615.1

Margirier, A., Braun, J., Gautheron, C., Carcaillet, J., Schwartz, S., Pinna Jamme, R., & Stanley, J. (2019). Climate control on Early Cenozoic denudation of the Namibian margin as deduced from new thermochronological constraints. *Earth and Planetary Science Letters*, 527. https://doi.org/10.1016/j.epsl.2019.115779

Meng, L., Li, Z.X., Chen, H., Li, X.H., & Wang, X.C. (2012). Geochronological and geochemical results from Mesozoic basalts in southern South China Block support the flat-slab subduction model. *Lithos*, 132–133, 127–140.

https://doi.org/10.1016/j.lithos.2011.11.022

Morinaga, H., & Liu, Y. Y. (2004). Cretaceous paleomagnetism of the eastern South China Block: establishment of the stable body of SCB. *Earth and Planetary Science Letters*, 222, 971–988. https://doi.org/10.1016/j.epsl.2004.02.035

Moser, A.C., Evans, J.P., Ault, A.K., Janecke, S.U., & Bradbury, K.K. (2017). (U–Th)/He thermochronometry reveals Pleistocene punctuated deformation and synkinematic hematite mineralization in the Mecca Hills, southernmost San Andreas Fault zone. *Earth and Planetary Science Letters*, 476, 87–99. https://doi.org/10.1016/j.epsl.2017.07.039

Qiu, L., Yan, D.P., Tang, S.L., Chen, F., Gong, L.X., & Zhang, Y.X. (2019). Cenozoic exhumation of the Neoproterozoic Sanfang batholith in South China. *Journal of the Geological Society*, 177. https://doi.org/10.1144/jgs2019-041

Reiners, P.W., & Farley, K.A. (2001). Influence of crystal size on apatite (U–Th)/He thermochronology: an example from the Bighorn Mountains, Wyoming. *Earth and Planetary Science Letters*, 188, 413–420. https://doi.org/10.1016/S0012-821X(01)00341-7

Reiners, P.W., Farley, K.A., & Hickes, H.J. (2002). He diffusion and (U–Th)/He thermochronometry of zircon: initial results from Fish Canyon Tuff and Gold Butte. *Tectonophysics*, 349, 297–308. https://doi.org/10.1016/S0040-1951(02)00058-6

Reiners, P.W., Spell, T., Nicolescu, S., & Zanetti, K. (2004). Zircon (U-Th)/He thermochronometry: He diffusion and comparisons with $^{40}Ar/^{39}Ar$ dating. *Geochimica et Cosmochimica Acta*, 68, 1857–1887. https://doi.org/10.1016/j.gca.2003.10.021

Reiners, P.W. (2005). Zircon (U-Th)/He Thermochronometry. *Reviews in Mineralogy and Geochemistry*, 58, 151–179. https://doi.org/10.2138/rmg.2005.58.6

Shu, L.S., Jahn, B.M., Charvet, J., Santosh, M., Wang, B., & Xu, X.S. (2014). Early Paleozoic depositional environment and intraplate tectono-magmatism in the Cathaysia block (south China): evidence from stratigraphic, structural,

geochemical and geochronological investigations. *American Journal of Science*, 314(1), 154–186. https://doi.org/10.2475/01.2014.05

Shu, L.S, Faure, M., Wang, B., Zhou, X., & Song, B. (2008). Late Palaeozoic–Early Mesozoic geological features of South China: Response to the Indosinian collision events in Southeast Asia. *Comptes Rendus Geoscience*, 340, 151–165. https://doi.org/10.1016/j.crte.2007.10.010

Shu, L.S., Zhou, X.M., Deng, P., Wang, B., Jiang, S.Y., Yu, J.H., & Zhao, X.X. (2009). Mesozoic tectonic evolution of the Southeast China Block: New insights from basin analysis. *Journal of Asian Earth Sciences*, 34, 376–391. https://doi.org/10.1016/j.jseaes.2008.06.004

Shu, X.J., Wang, X.L., Sun, T., Xu, X., & Dai, M.N. (2011). Trace elements, U–Pb ages and Hf isotopes of zircons from Mesozoic granites in the western Nanling Range, South China: Implications for petrogenesis and W–Sn mineralization. *Lithos*, 127, 468–482. https://doi.org/10.1016/j.lithos.2011.09.019

Shuster, D.L., Flowers, R.M., & Farley, K.A. (2006). The influence of natural radiation damage on helium diffusion kinetics in apatite. *Earth and Planetary Science Letters*, 249, 148–161. https://doi.org/10.1016/j.epsl.2006.07.028

Sillitoe, R., & Perelló, J. (2005). Andean copper province: Tectonomagmatic settings, deposit types, metallogeny, exploration, and discovery. *Economic Geology 100th Anniversary Volume*, 845–890.

Sillitoe, R. (2010). Porphyry Copper Systems. *Economic Geology*, 105, 3–41. https://doi.org/10.2113/gsecongeo.105.1.3

Song, M., Shu, L., Santosh, M., & Li, J. (2015). Late Early Paleozoic and Early Mesozoic intracontinental orogeny in the South China Craton: Geochronological and geochemical evidence. *Lithos*, 232, 360–374. https://doi.org/10.1016/j.lithos.2015.06.019

Stalder, N.F., Herman, F., Fellin, M.G., Coutand, I., Aguilar, G., Reiners, P.W., & Fox, M., (2020). The relationships between tectonics, climate and exhumation in the Central Andes (18–36°S): Evidence from low-temperature thermochronology.

Earth-Science Reviews, 210. https://doi.org/10.1016/j.earscirev.2020.103276

Su, J., Dong, S., Zhang, Y., Li, Y., Chen, X., Li, J., Cui, J., & Chen, J. (2017). Apatite fission track geochronology of the Southern Hunan province across the Shi-Hang Belt: insights into the Cenozoic dynamic topography of South China. *International Geology Review*, 59, 981–995. https://doi.org/10.1080/00206814.2016.1240049

Sun, L.Q., Ling, H.F., Shen, W.Z., Wang, K.X., & Huang, G.L. (2017). Petrogenesis of two Triassic A-type intrusions in the interior of South China and their implications for tectonic transition. *Lithos*, 284-285, 642–653. https://doi.org/10.1016/j.lithos.2017.05.006

Sun, Y., Chen, Z., Boone, S.C., Zhong, F., & Tao, W., (2021). Exhumation history and preservation of the Changjiang uranium ore field, South China, revealed by (U-Th)/He and fission track thermochronology. *Ore Geology Reviews*, 133. https://doi.org/10.1016/j.oregeorev.2021.104101

Sun, Z., Yang, Z., Yang, T., Pei, J., & Yu, Q. (2006). New Late Cretaceous and Paleogene paleomagnetic results from South China and their geodynamic implications. *Journal of Geophysical Research*, 111. https://doi.org/10.1029/2004JB003455

Tang, S.L., Yan, D.P., Qiu, L., Gao, J.F., & Wang, C.L. (2014). Partitioning of the Cretaceous Pan-Yangtze Basin in the central South China Block by exhumation of the Xuefeng Mountains during a transition from extensional to compressional tectonics? *Gondwana Research*, 25, 1644–1659. https://doi.org/10.1016/j.gr.2013.06.014

Tao, N., Li, Z.X., Danišík, M., Evans, N.J., Batt, G.E., Li, W.X., Pang, C.J., Jourdan, F., Xu, Y.G., & Liu, L.P. (2017). Thermochronological record of Middle–Late Jurassic magmatic reheating to Eocene rift-related rapid cooling in the SE South China Block. *Gondwana Research*, 46, 191–203. https://doi.org/10.1016/j.gr.2017.03.003

Tao, N., Li, Z.X., Danišík, M., Evans, N.J., Li, R.X., Pang, C.J., Li, W.X., Jourdan, F.,

1100 Yu, Q., Liu, L.P., Batt, G.E., & Xu, Y.G. (2019). Post-250 Ma thermal evolution
1101 of the central Cathaysia Block (SE China) in response to flat-slab subduction at
1102 the proto-Western Pacific margin. *Gondwana Research*, 75, 1–15.
1103 https://doi.org/10.1016/j.gr.2019.03.019
1104 Vermeesch, P. (2008). Three new ways to calculate average (U–Th)/He ages.
1105 *Chemical Geology*, 249, 339–347.
1106 https://doi.org/10.1016/j.chemgeo.2008.01.027
1107 Vermeesch, P. (2010). HelioPlot, and the treatment of overdispersed (U–Th–Sm)/He
1108 data. *Chemical Geology*, 271, 108–111.
1109 https://doi.org/10.1016/j.chemgeo.2010.01.002
1110 Vermeesch, P., & Tian, Y. (2014). Thermal history modelling: HeFTy vs. QTQt.
1111 *Earth-Science Reviews*, 139. https://doi.org/10.1016/j.earscirev.2014.09.010
1112 Vermeesch, P. (2018). IsoplotR: A free and open toolbox for geochronology.
1113 *Geoscience Frontiers*, 9, 1479–1493. https://doi.org/10.1016/j.gsf.2018.04.001
1114 Wang, F., Chen, H., Batt, G.E., Lin, X., Gong, J., Gong, G., Meng, L., Yang, S., &
1115 Jourdan, F. (2015). Tectonothermal history of the NE Jiangshan–Shaoxing suture
1116 zone: Evidence from $^{40}Ar/^{39}Ar$ and fission-track thermochronology in the
1117 Chencai region. *Precambrian Research*, 264, 192–203.
1118 https://doi.org/10.1016/j.precamres.2015.04.009
1119 Wang, X.Y., Suo, Y.H., Li, S.Z., Cao, X.Z., Li, X.Y., Zhou, J., Wang P.C., & Jin, C.,
1120 (2020b). Cenozoic uplift history and its dynamic mechanism along the eastern
1121 continental margin of South China. *Acta Petrologica Sinica*, 36(6), 1803–1820.
1122 (in Chinese with English abstract)
1123 Wang, Y., Fan, W., Guo, F., Peng, T., & Li, C. (2010). Geochemistry of Mesozoic
1124 Mafic Rocks Adjacent to the Chenzhou-Linwu fault, South China: Implications
1125 for the Lithospheric Boundary between the Yangtze and Cathaysia Blocks.
1126 *International Geology Review*, 45, 263–286.
1127 https://doi.org/10.2747/0020-6814.45.3.263
1128 Wang, Y., Fan, W., Guo, F., Peng, T., & Li, C. (2003). Geochemistry of Mesozoic

Mafic Rocks Adjacent to the Chenzhou-Linwu fault, South China: Implications for the Lithospheric Boundary between the Yangtze and Cathaysia Blocks. *International Geology Review*, 45, 263–286. https://doi.org/10.2747/0020-6814.45.3.263

Wang, Y., Fan, W., Zhang, G., & Zhang, Y. (2013). Phanerozoic *Tectonics*, of the South China Block: Key observations and controversies. *Gondwana Research*, 23, 1273–1305. https://doi.org/10.1016/j.gr.2012.02.019

Wang, Y., Zhang, J., Zhang, B., & Zhao, H. (2018). Cenozoic exhumation history of South China: A case study from the Xuefeng Mt. Range. *Journal of Asian Earth Sciences*, 151, 173–189. https://doi.org/10.1016/j.jseaes.2017.10.039

Wang, Y.J, Wang, Y.J., Li, S., Seagren, E., Zhang, Y., Zhang, P., & Qian, X., (2020). Exhumation and landscape evolution in eastern South China since the Cretaceous: New insights from fission-track thermochronology. *Journal of Asian Earth Sciences*, 191. https://doi.org/10.1016/j.jseaes.2020.104239

Wang, Y.J., Wang, Y., Zhang, Y., Cawood, P.A., Qian, X., Gan, C., Zhang, F., & Zhang, P., (2021). Triassic two-stage intra-continental orogensis of the South China Block, driven by Paleotethyan closure and interactions with adjoining blocks. *Journal of Asian Earth Sciences*, 206. https://doi.org/10.1016/j.jseaes.2020.104648

Wolf, R.A., Farley, K.A., & Silver, L.T. (1996). Helium diffusion and low-temperature thermochronometry of apatite. *Geochimica et Cosmochimica Acta*, 60, 4231–4240. https://doi.org/10.1016/S0016-7037(96)00192-5

Wu, F.Y., Ji, W.Q., Sun, D.H., Yang, Y.H., & Li, X.H. (2012). Zircon U-Pb geochronology and Hf isotopic compositions of the Mesozoic granites in southern Anhui Province, China. *Lithos*, 150, 6–25. https://doi.org/10.1016/j.lithos.2012.03.020

Wu, J.H., Li, H., Algeo, T.J., Jiang, W.C., & Zhou, Z.K. (2018). Genesis of the Xianghualing Sn–Pb–Zn deposit, South China: A multi-method zircon study. *Ore Geology Reviews*, 102, 220–239. https://doi.org/10.1016/j.oregeorev.2018.09.005

Wu, Y.B., & Zheng, Y.F. (2013). Tectonic evolution of a composite collision orogen: An overview on the Qinling-Tongbai-Hong'an-Dabie-Sulu orogenic belt in central China. *Gondwana Research*, 23, 1402–1428. https://doi.org/10.1016/j.gr.2012.09.007

Willett, C.D., Fox, M., & Shuster, D.L. (2017). A helium-based model for the effects of radiation damage annealing on helium diffusion kinetics in apatite. *Earth and Planetary Science Letters*, 477, 195–204. https://doi.org/10.1016/j.epsl.2017.07.047

Xia, Y., Xu, X.S., & Zhu, K.Y. (2012). Paleoproterozoic S- and A-type granites in southwestern Zhejiang: magmatism, metamorphism and implications for the crustal evolution of the Cathaysia basement. *Precambrian Research*, 216-219, 177–207. https://doi.org/10.1016/j.precamres.2012.07.001

Xia, Y., & Xu, X. (2020). The epilogue of Paleo-Tethyan *Tectonics*, in the South China Block: Insights from the Triassic aluminous A-type granitic and bimodal magmatism. *Journal of Asian Earth Sciences*, 190. https://doi.org/10.1016/j.jseaes.2019.104129

Xie, Y., Wu, F., & Fang, X. (2019). Middle Eocene East Asian monsoon prevalence over southern China: Evidence from palynological records. *Global and Planetary Change*, 175, 13–26. https://doi.org/10.1016/j.gloplacha.2019.01.019

Xie, Y., Wu, F., Fang, X., Zhang, D., & Zhang, W. (2020). Early Eocene southern China dominated by desert: Evidence from a palynological record of the Hengyang Basin, Hunan Province. *Global and Planetary Change*, 195. https://doi.org/10.1016/j.gloplacha.2020.103320

Yamaji, A. (2000). The multiple inverse method applied to meso–scale faults in mid–Quaternary fore–arc sediments near the triple trench junction off central Japan. *Journal of Structural Geology*, 22, 429–440. https://doi.org/10.1016/S0191-8141(99)00162-5

Yan, Y., Hu, X., Lin, G., Santosh, M., & Chan, L.S. (2011). Sedimentary provenance of the Hengyang and Mayang basins, SE China, and implications for the

Mesozoic topographic change in South China Craton: Evidence from detrital zircon geochronology. *Journal of Asian Earth Sciences*, 41, 494–503. https://doi.org/10.1016/j.jseaes.2011.03.012

Yao, J., Cawood, P.A., Shu, L., & Zhao, G. (2019). Jiangnan Orogen, South China: A ~970–820 Ma Rodinia margin accretionary belt. *Earth-Science Reviews*, 196. https://doi.org/10.1016/j.earscirev.2019.05.016

Yi, Y., Carter, A., Xia, B., Ge, L., Brichau, S., & Hu, X.Q. (2009). A fission-track and (U–Th)/He thermochronometric study of the northern margin of the South China Sea: An example of a complex passive margin. *Tectonophysics*, 474, 584–594. https://doi.org/10.1016/j.tecto.2009.04.030

Yin, Y., Jin, S., Wei, W., Lü, Q., Ye, G., Jing, J., Zhang, L., Dong, H., & Xie, C. (2021). Lithosphere structure and its implications for the metallogenesis of the Nanling Range, South China: Constraints from 3-D magnetotelluric imaging. *Ore Geology Reviews*, 131. https://doi.org/10.1016/j.oregeorev.2021.104064

Yu, J.H., O'Reilly, S.Y., Zhou, M.F., Griffin, W.L., & Wang, L. (2012). U–Pb geochronology and Hf–Nd isotopic geochemistry of the Badu complex, southeastern China: implications for the Precambrian crustal evolution and paleogeography of the Cathaysia block. *Precambrian Research*, 222-223, 424–449. https://doi.org/10.1016/j.precamres.2011.07.014

Yuan, S., Williams-Jones, A., Romer, R., Zhao, P., & Mao, J. (2019). Protolith-Related Thermal Controls on the Decoupling of Sn and W in Sn-W Metallogenic Provinces: Insights from the Nanling Region, China. *Economic Geology*, 114, 1005–1012. https://doi.org/10.5382/econgeo.4669

Zhang, R.Q., Lu, J.J., Wang, R.C., Yang, P., Zhu, J.C., Yao, Y., Gao, J.F., Li, C., Lei, Z.H., Zhang, W.L., & Guo, W.M. (2015). Constraints of in situ zircon and cassiterite U–Pb, molybdenite Re–Os and muscovite 40Ar–39Ar ages on multiple generations of granitic magmatism and related W–Sn mineralization in the Wangxianling area, Nanling Range, South China. *Ore Geology Reviews*, 65, 1021–1042. https://doi.org/10.1016/j.oregeorev.2014.09.021

Zhang, Z., Ning, Y., Lu, Y., Cao, J., Fu, J., Zhao, Z., Guo, J., Ma, L., Qin, Z., & Li, J. (2021). Geological characteristics and metallogenic age of Tengshan'ao Sn deposit in Dayishan of South Hunan and its prospecting significance. *Solid Earth Sciences*, 6, 37–49. https://doi.org/10.1016/j.sesci.2021.01.002

Zhong, J., Pirajno, F., & Chen, Y. J. (2017). Epithermal deposits in South China: Geology, geochemistry, geochronology and tectonic setting. *Gondwana Research*, 42, 193–219. https://doi.org/10.1016/j.gr.2016.10.008

Zhou, X.M., Shen, W.Z., Shu, L.S., & Niu, Y.L. (2006). Petrogenesis of Mesozoic granitoids and volcanic rocks in south china: a response to tectonic evolution. *Episodes*, 29 (1), 26–33. https://doi.org/10.18814/epiiugs/2006/v29i1/004

Zhou, X.M., & Li, W.X. (2000). Origin of late Mesozoic igneous rocks in southeastern China: implications for lithosphere subduction and underplating of mafic magmas. *Tectonophysics*, 326 (3), 269–287. https://doi.org/10.1016/S0040-1951(00)00120-7

Figure 1.

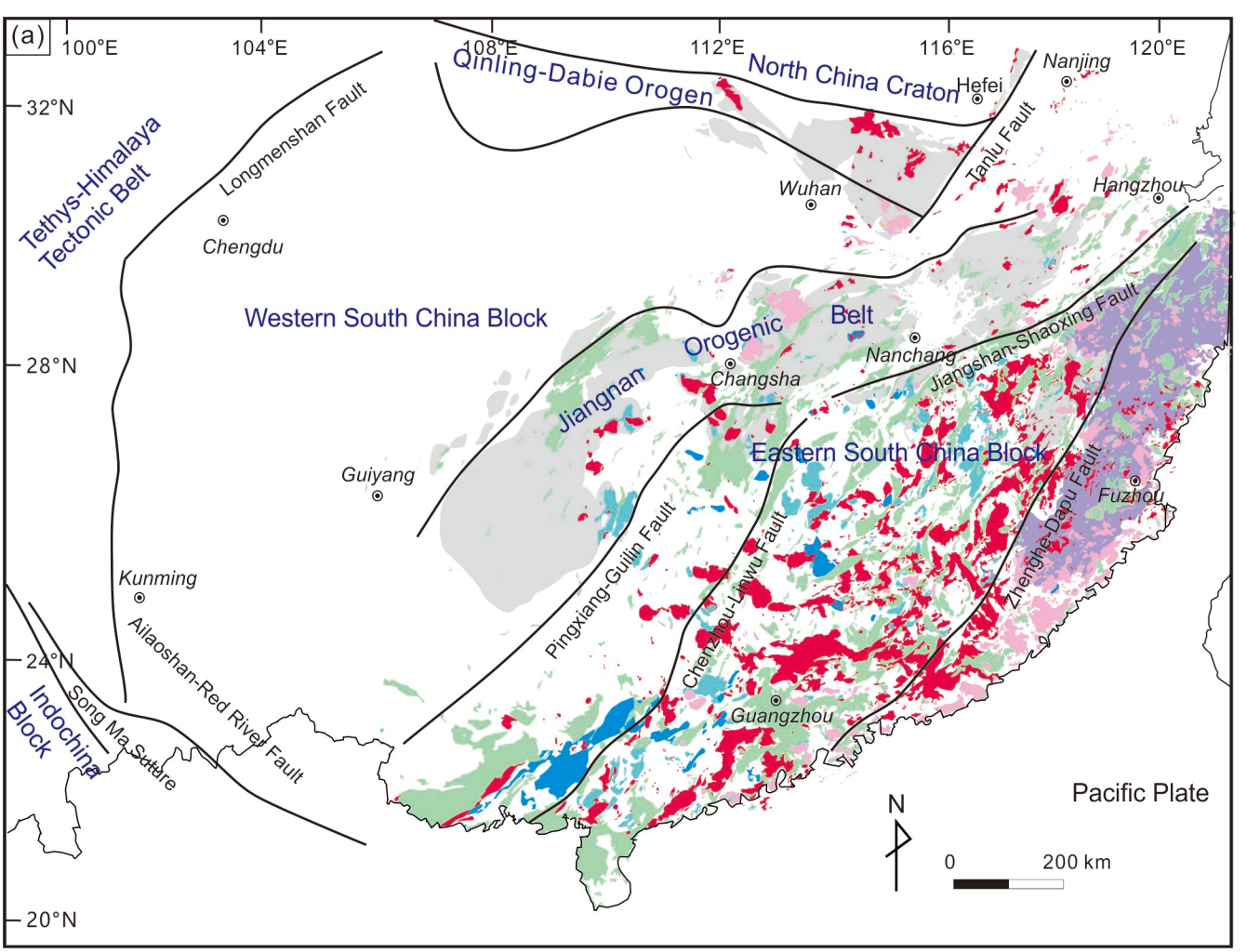
(a)
100°E
104°E
108°E
112°E
116°E
120°E
32°N
28°N
24°N
20°N
Qinling-Dabie Orogen
North China Craton
Tanlu Fault
Hefei
Nanjing
Wuhan
Hangzhou
Tethys-Himalaya Tectonic Belt
Longmenshan Fault
Chengdu
Western South China Block
Orogenic Belt
Jiangnan
Nanchang
Changsha
Jiangshan-Shaoxing Fault
Eastern South China Block
Guiyang
Fuzhou
Zhenghe-Dapu Fault
Pingxiang-Guilin Fault
Chenzhou-Linwu Fault
Kunming
Ailaoshan-Red River Fault
Song Ma Suture
Indochina Block
Guangzhou
Pacific Plate
N
0
200 km
Cretaceous volcanic rocks
Cretaceous granites
Jurassic granites
Jurassic to Cretaceous sedimentary rocks
Triassic granites
Early Plaeozoic granites
Precambrian basement
Major faults
Major cities

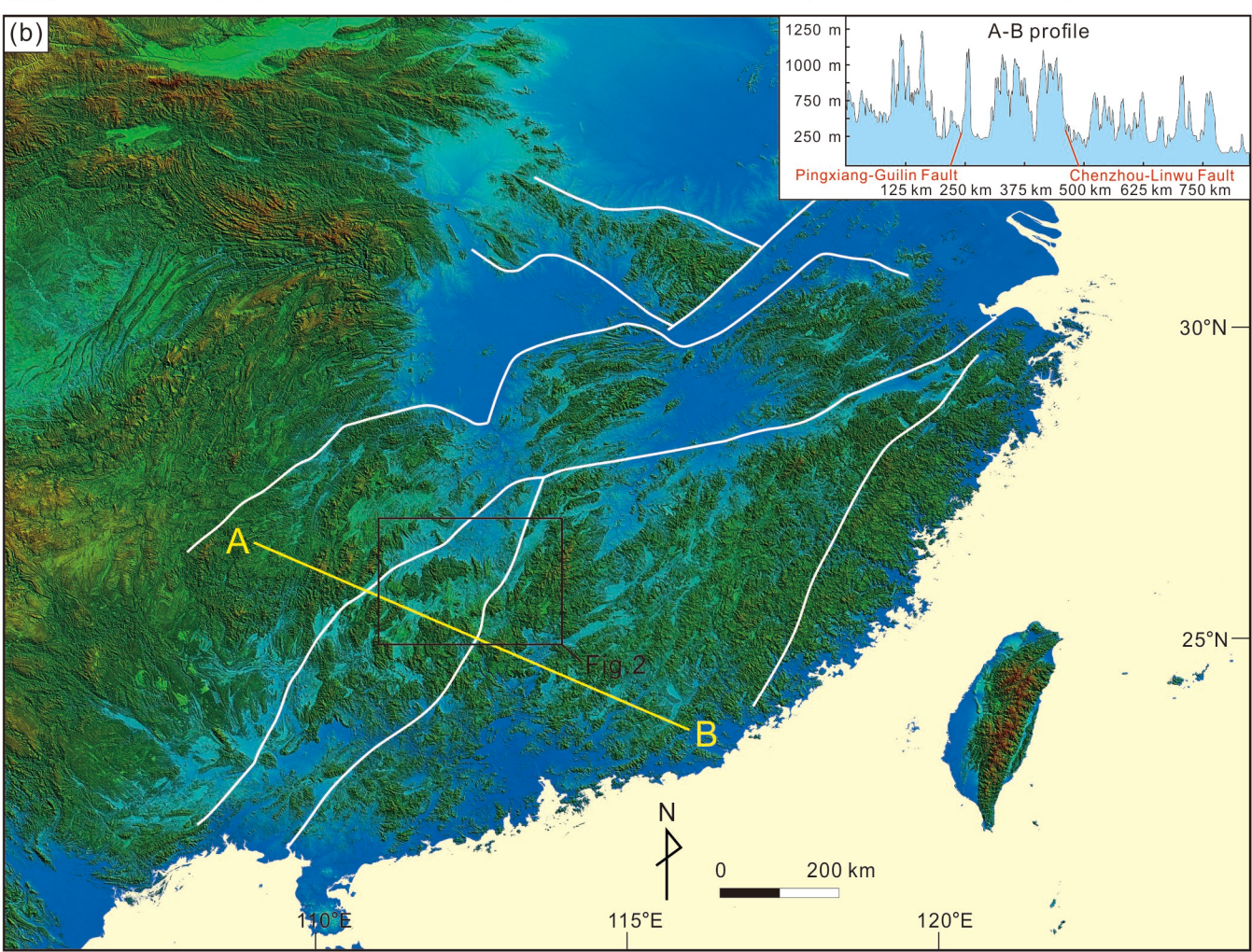
(b)
A-B profile
1250 m
1000 m
750 m
250 m
Pingxiang-Guilin Fault
Chenzhou-Linwu Fault
125 km 250 km 375 km 500 km 625 km 750 km
A
B
Fig. 2
30°N
25°N
N
0
200 km
110°E
115°E
120°E

Figure 2.

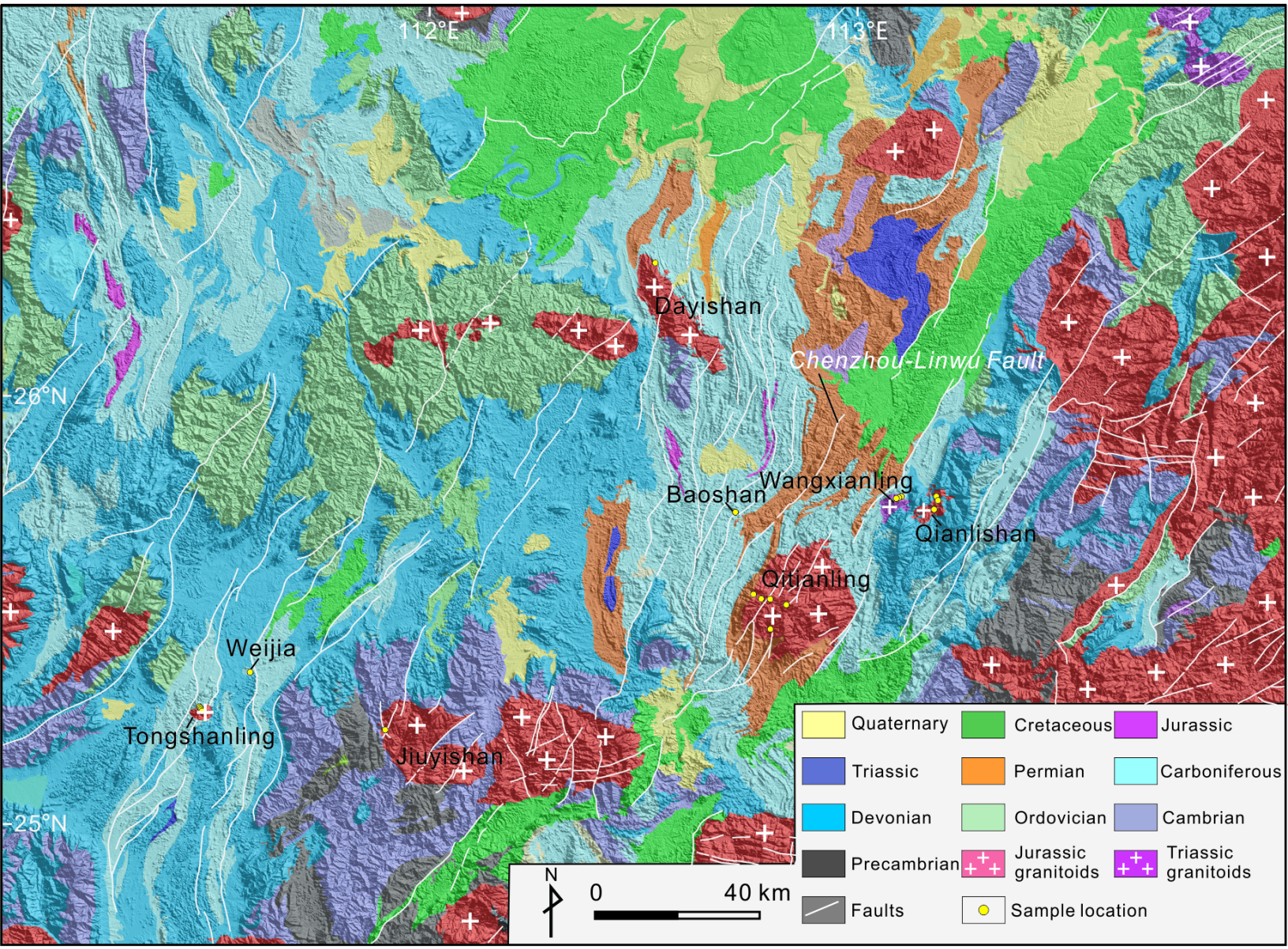
112°E
113°E
26°N
25°N
Dayishan
Chenzhou-Linwu Fault
Wangxianling
Baoshan
Qianlishan
Qitianling
Weijia
Tongshanling
Jiuyishan
N
0
40 km
Quaternary
Cretaceous
Jurassic
Triassic
Permian
Carboniferous
Devonian
Ordovician
Cambrian
Precambrian
Jurassic granitoids
Triassic granitoids
Faults
Sample location

Figure 3.

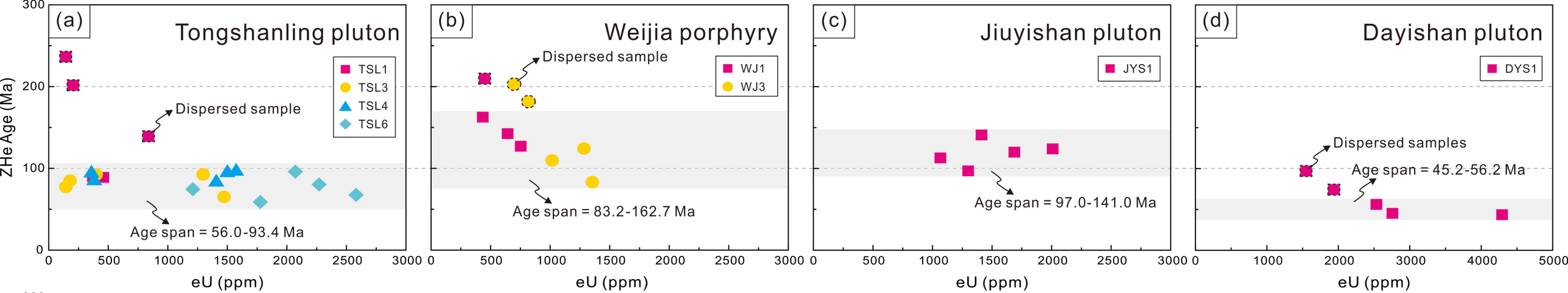
(a)
Tongshanling pluton
TSL1
TSL3
TSL4
TSL6
Dispersed sample
Age span = 56.0-93.4 Ma
(b)
Weijia porphyry
WJ1
WJ3
Dispersed sample
Age span = 83.2-162.7 Ma
(c)
Jiuyishan pluton
JYS1
Age span = 97.0-141.0 Ma
(d)
Dayishan pluton
DYS1
Dispersed samples
Age span = 45.2-56.2 Ma
(e)
Baoshan porphyry
BS1
BS2
BS3
Age span = 115.9-148.4 Ma
Dispersed sample
(f)
Qitianling pluton
QTL1
QTL2
QTL5
QTL6
QTL7
Dispersed sample
Age span = 64.3-103.3 Ma
(g)
Wangxianling pluton
WXL1
WXL5
WXL6
Age span = 28.3-82.4 Ma
Dispersed sample
(h)
Qianlishan pluton
QLS1
QLS2
Dispersed sample
Age span = 77.2-95.6 Ma
ZHe Age (Ma)
eU (ppm)

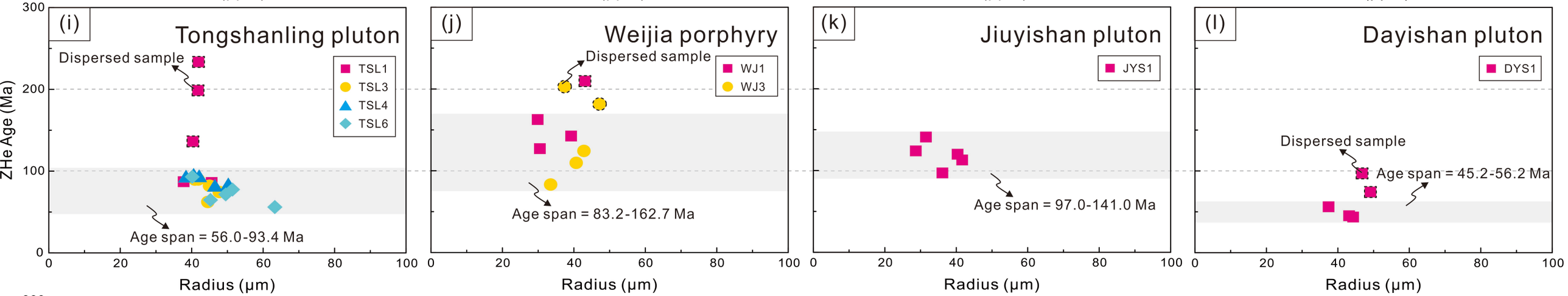
(i)
Tongshanling pluton
TSL1
TSL3
TSL4
TSL6
Dispersed sample
Age span = 56.0-93.4 Ma
(j)
Weijia porphyry
WJ1
WJ3
Dispersed sample
Age span = 83.2-162.7 Ma
(k)
Jiuyishan pluton
JYS1
Age span = 97.0-141.0 Ma
(l)
Dayishan pluton
DYS1
Dispersed sample
Age span = 45.2-56.2 Ma
(m)
Baoshan porphyry
BS1
BS2
BS3
Age span = 115.9-148.4 Ma
Dispersed sample
(n)
Qitianling pluton
QTL1
QTL2
QTL5
QTL6
QTL7
Dispersed sample
Age span = 64.3-103.3 Ma
(o)
Wangxianling pluton
WXL1
WXL5
WXL6
Age span = 28.3-82.4 Ma
Dispersed sample
(p)
Qianlishan pluton
QLS1
QLS2
Dispersed sample
Age span = 77.2-95.6 Ma
ZHe Age (Ma)
Radius (μm)

Figure 4.

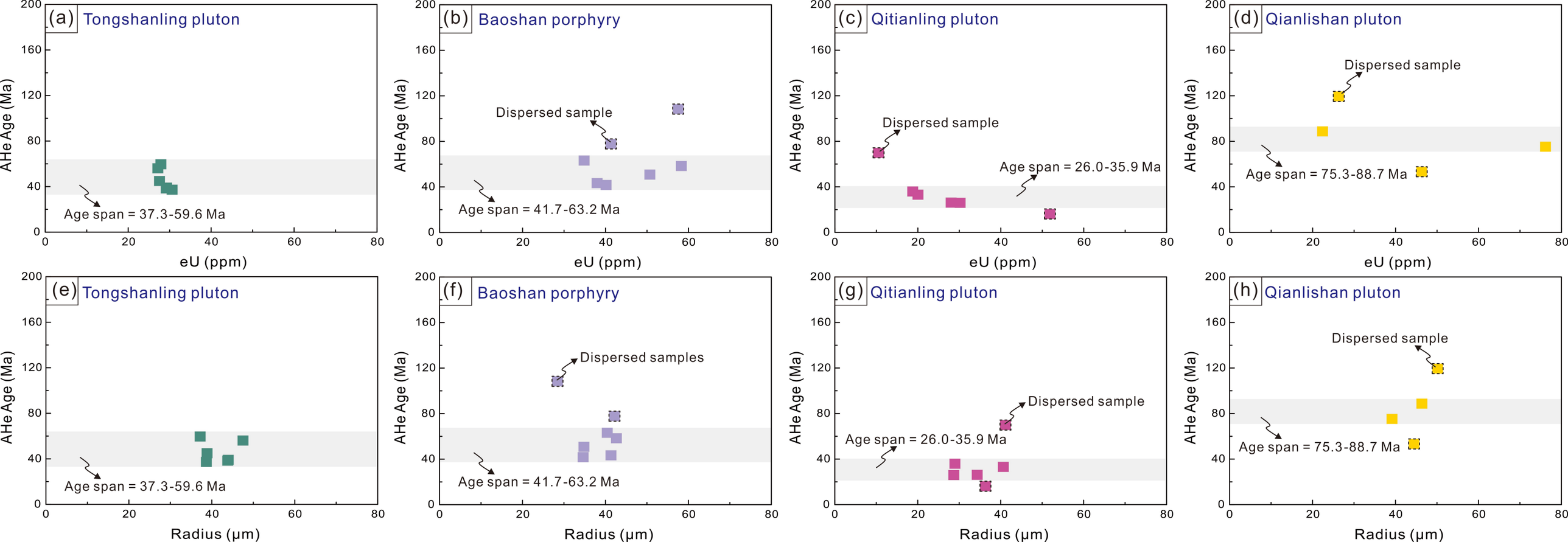
(a) Tongshanling pluton
Age span = 37.3-59.6 Ma
(b) Baoshan porphyry
Dispersed sample
Age span = 41.7-63.2 Ma
(c) Qitianling pluton
Dispersed sample
Age span = 26.0-35.9 Ma
(d) Qianlishan pluton
Dispersed sample
Age span = 75.3-88.7 Ma
(e) Tongshanling pluton
Age span = 37.3-59.6 Ma
(f) Baoshan porphyry
Dispersed samples
Age span = 41.7-63.2 Ma
(g) Qitianling pluton
Dispersed sample
Age span = 26.0-35.9 Ma
(h) Qianlishan pluton
Dispersed sample
Age span = 75.3-88.7 Ma
AHe Age (Ma)
eU (ppm)
Radius (μm)

Figure 5.

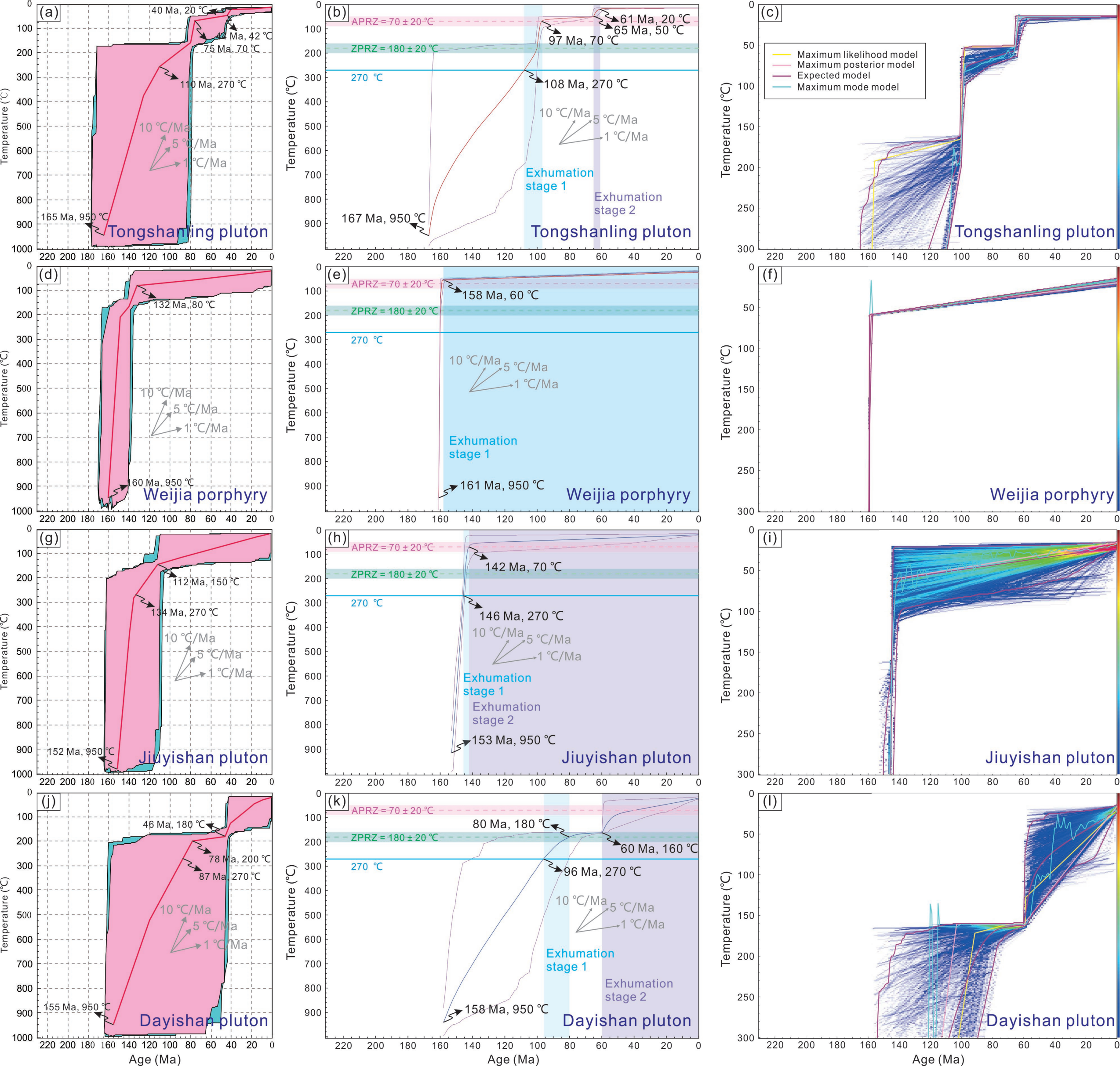
(a)
40 Ma, 20 ℃
44 Ma, 42 ℃
75 Ma, 70 ℃
110 Ma, 270 ℃
10 ℃/Ma
5 ℃/Ma
1 ℃/Ma
165 Ma, 950 ℃
Tongshanling pluton
(b)
APRZ = 70 ± 20 ℃
ZPRZ = 180 ± 20 ℃
270 ℃
61 Ma, 20 ℃
65 Ma, 50 ℃
97 Ma, 70 ℃
108 Ma, 270 ℃
10 ℃/Ma
5 ℃/Ma
1 ℃/Ma
Exhumation stage 1
Exhumation stage 2
167 Ma, 950 ℃
Tongshanling pluton
(c)
Maximum likelihood model
Maximum posterior model
Expected model
Maximum mode model
Tongshanling pluton
(d)
132 Ma, 80 ℃
10 ℃/Ma
5 ℃/Ma
1 ℃/Ma
160 Ma, 950 ℃
Weijia porphyry
(e)
APRZ = 70 ± 20 ℃
ZPRZ = 180 ± 20 ℃
270 ℃
158 Ma, 60 ℃
10 ℃/Ma
5 ℃/Ma
1 ℃/Ma
Exhumation stage 1
161 Ma, 950 ℃
Weijia porphyry
(f)
Weijia porphyry
(g)
112 Ma, 150 ℃
134 Ma, 270 ℃
10 ℃/Ma
5 ℃/Ma
1 ℃/Ma
152 Ma, 950 ℃
Jiuyishan pluton
(h)
APRZ = 70 ± 20 ℃
ZPRZ = 180 ± 20 ℃
270 ℃
142 Ma, 70 ℃
146 Ma, 270 ℃
10 ℃/Ma
5 ℃/Ma
1 ℃/Ma
Exhumation stage 1
Exhumation stage 2
153 Ma, 950 ℃
Jiuyishan pluton
(i)
Jiuyishan pluton
(j)
46 Ma, 180 ℃
78 Ma, 200 ℃
87 Ma, 270 ℃
10 ℃/Ma
5 ℃/Ma
1 ℃/Ma
155 Ma, 950 ℃
Dayishan pluton
(k)
APRZ = 70 ± 20 ℃
ZPRZ = 180 ± 20 ℃
270 ℃
80 Ma, 180 ℃
60 Ma, 160 ℃
96 Ma, 270 ℃
10 ℃/Ma
5 ℃/Ma
1 ℃/Ma
Exhumation stage 1
Exhumation stage 2
158 Ma, 950 ℃
Dayishan pluton
(l)
Dayishan pluton
Temperature (℃)
Age (Ma)

Figure 6.

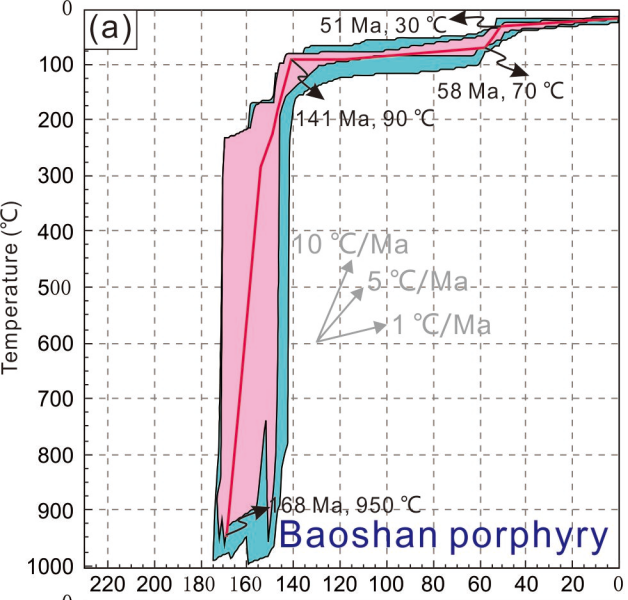
(a)
51 Ma, 30 ℃
58 Ma, 70 ℃
141 Ma, 90 ℃
10 ℃/Ma
5 ℃/Ma
1 ℃/Ma
168 Ma, 950 ℃
Baoshan porphyry
Temperature (℃)

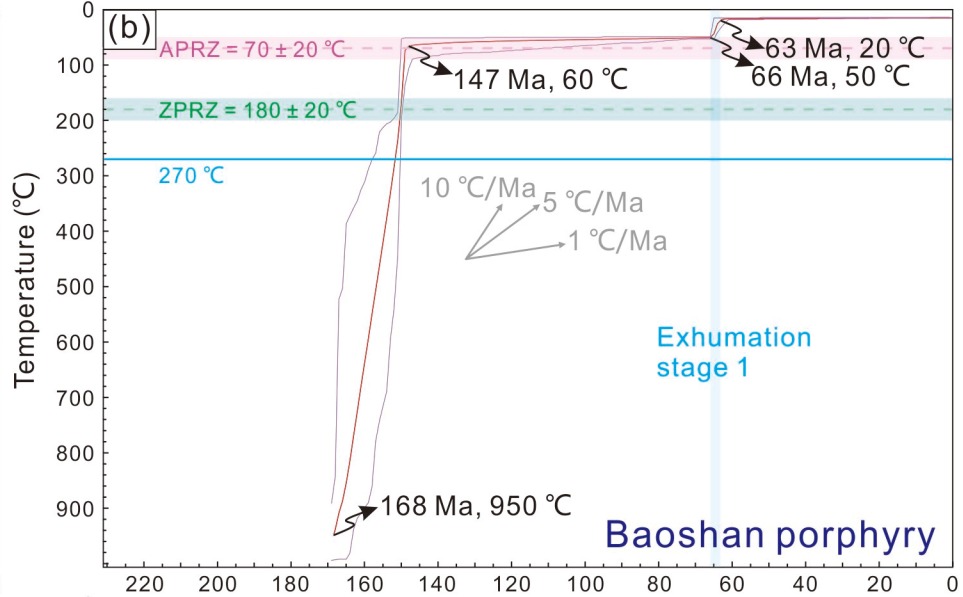
(b)
APRZ = 70 ± 20 ℃
ZPRZ = 180 ± 20 ℃
270 ℃
147 Ma, 60 ℃
63 Ma, 20 ℃
66 Ma, 50 ℃
10 ℃/Ma
5 ℃/Ma
1 ℃/Ma
Exhumation stage 1
168 Ma, 950 ℃
Baoshan porphyry
Temperature (℃)

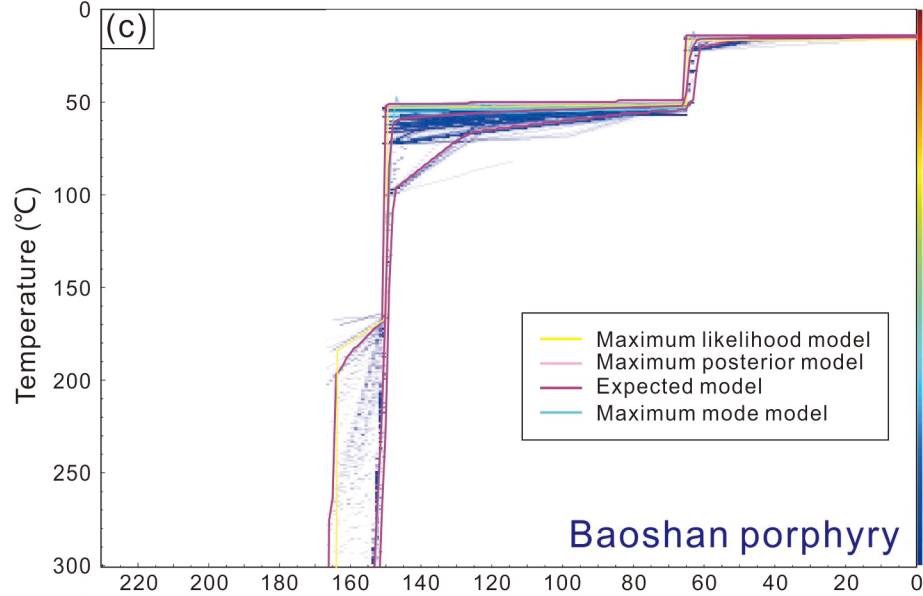
(c)
Maximum likelihood model
Maximum posterior model
Expected model
Maximum mode model
Baoshan porphyry
Temperature (℃)

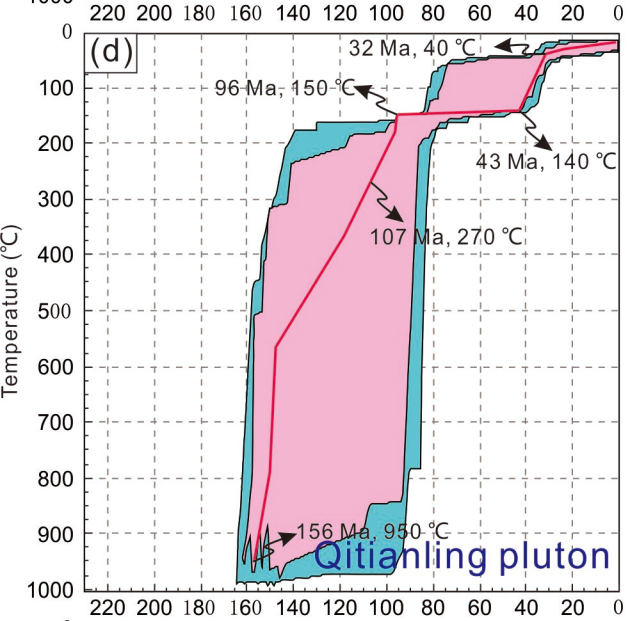
(d)
32 Ma, 40 ℃
96 Ma, 150 ℃
43 Ma, 140 ℃
107 Ma, 270 ℃
156 Ma, 950 ℃
Qitianling pluton
Temperature (℃)

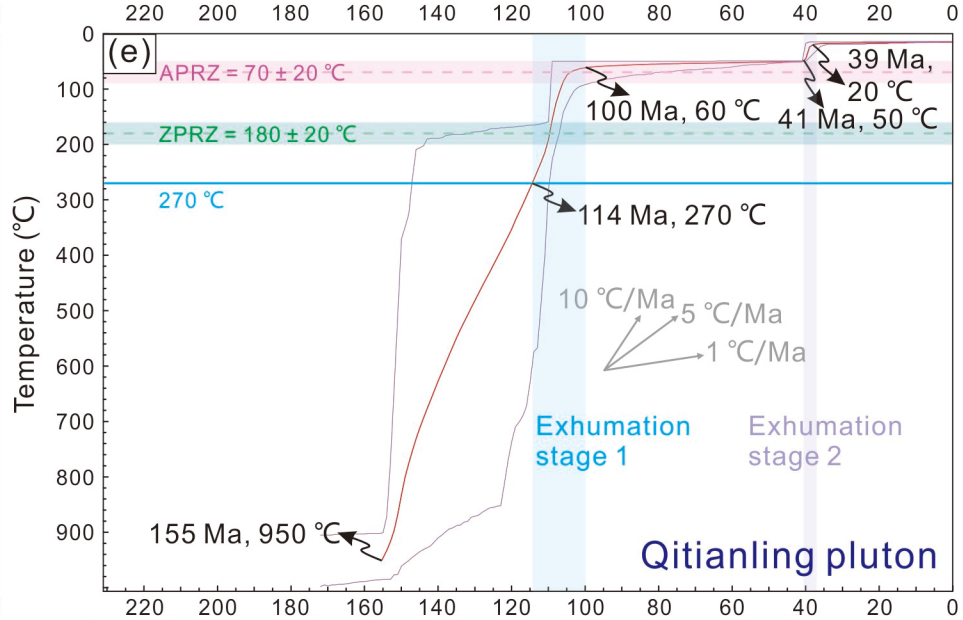
(e)
APRZ = 70 ± 20 ℃
ZPRZ = 180 ± 20 ℃
270 ℃
100 Ma, 60 ℃
39 Ma, 20 ℃
41 Ma, 50 ℃
114 Ma, 270 ℃
10 ℃/Ma
5 ℃/Ma
1 ℃/Ma
Exhumation stage 1
Exhumation stage 2
155 Ma, 950 ℃
Qitianling pluton
Temperature (℃)

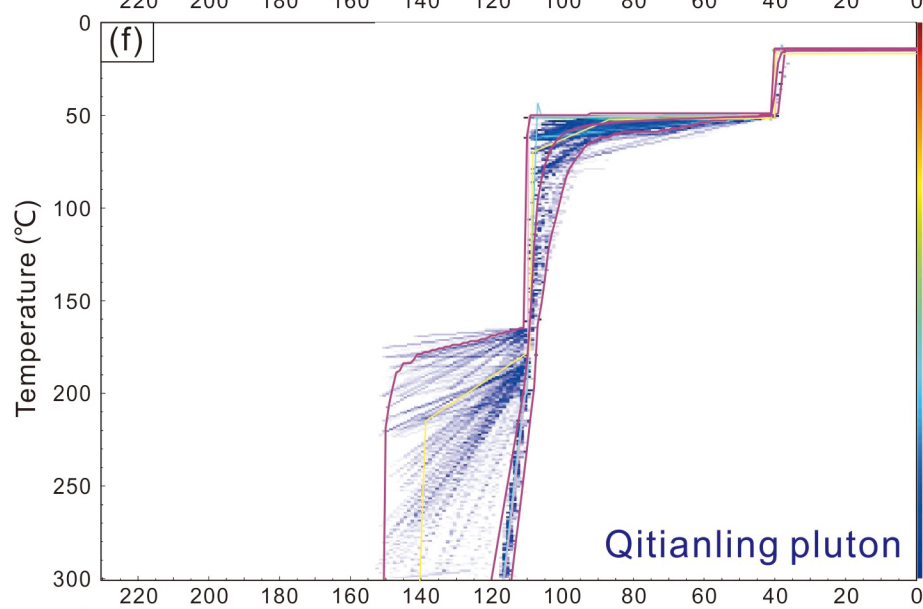
(f)
Qitianling pluton
Temperature (℃)

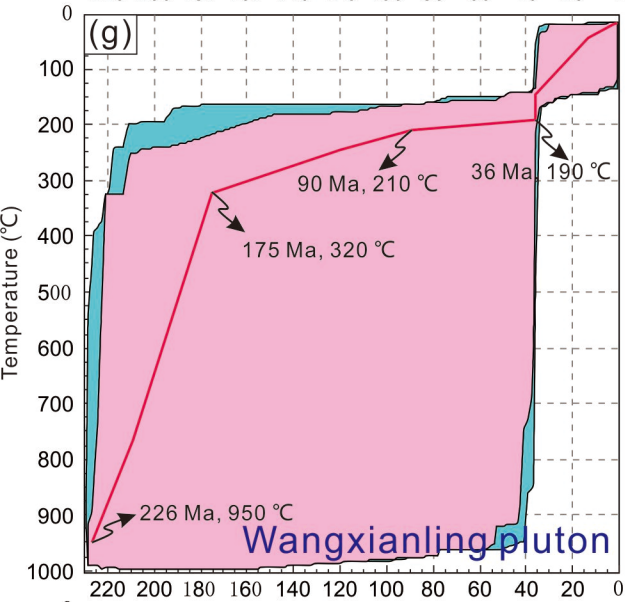
(g)
90 Ma, 210 ℃
36 Ma, 190 ℃
175 Ma, 320 ℃
226 Ma, 950 ℃
Wangxianling pluton
Temperature (℃)

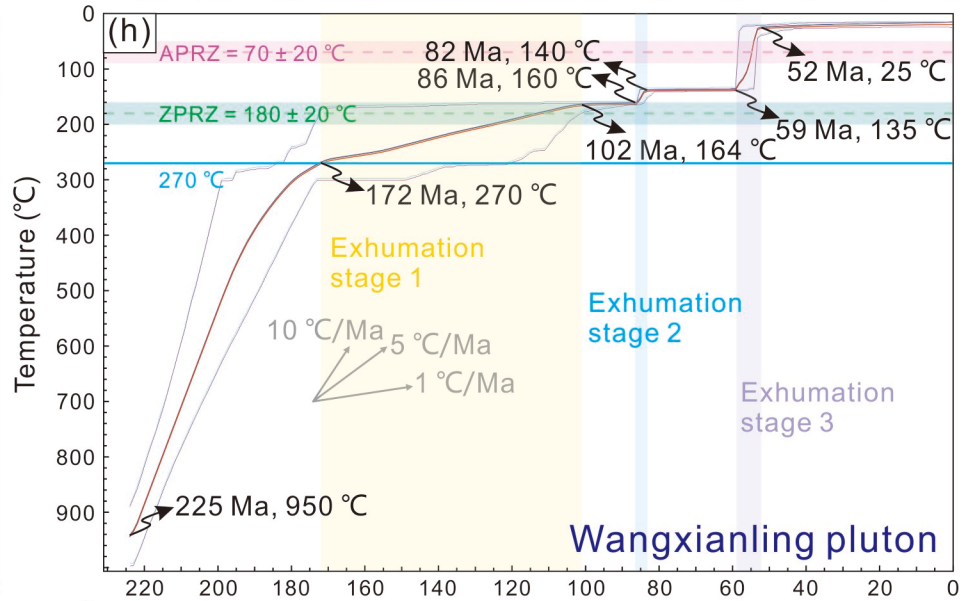
(h)
APRZ = 70 ± 20 ℃
ZPRZ = 180 ± 20 ℃
270 ℃
82 Ma, 140 ℃
86 Ma, 160 ℃
52 Ma, 25 ℃
59 Ma, 135 ℃
102 Ma, 164 ℃
172 Ma, 270 ℃
Exhumation stage 1
Exhumation stage 2
Exhumation stage 3
10 ℃/Ma
5 ℃/Ma
1 ℃/Ma
225 Ma, 950 ℃
Wangxianling pluton
Temperature (℃)

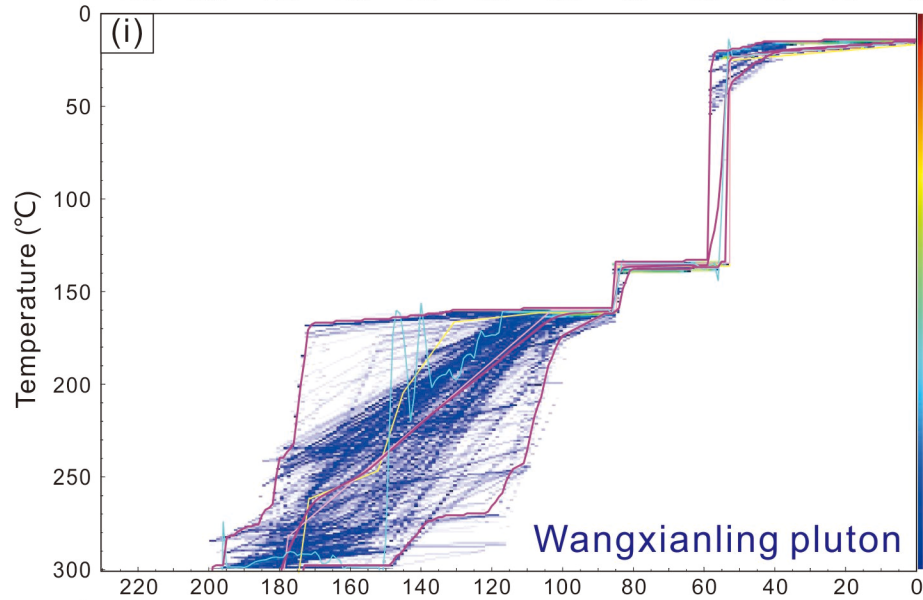
(i)
Wangxianling pluton
Temperature (℃)

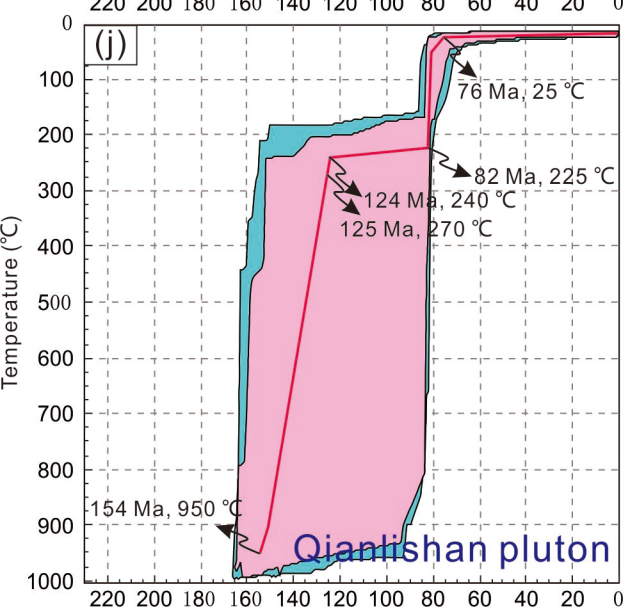
(j)
76 Ma, 25 ℃
82 Ma, 225 ℃
124 Ma, 240 ℃
125 Ma, 270 ℃
154 Ma, 950 ℃
Qianlishan pluton
Temperature (℃)

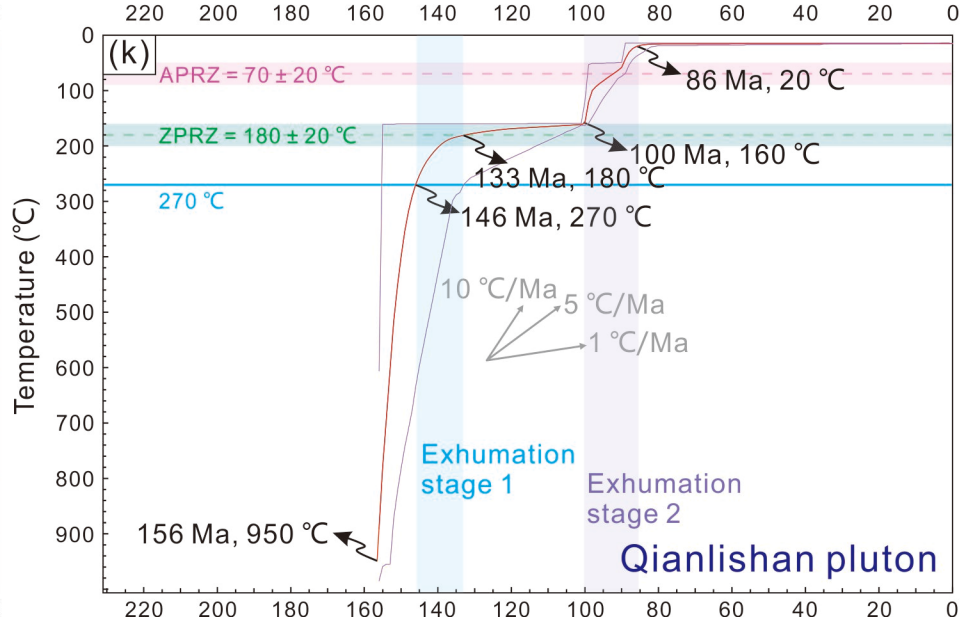
(k)
APRZ = 70 ± 20 ℃
ZPRZ = 180 ± 20 ℃
270 ℃
86 Ma, 20 ℃
100 Ma, 160 ℃
133 Ma, 180 ℃
146 Ma, 270 ℃
10 ℃/Ma
5 ℃/Ma
1 ℃/Ma
Exhumation stage 1
Exhumation stage 2
156 Ma, 950 ℃
Qianlishan pluton
Temperature (℃)

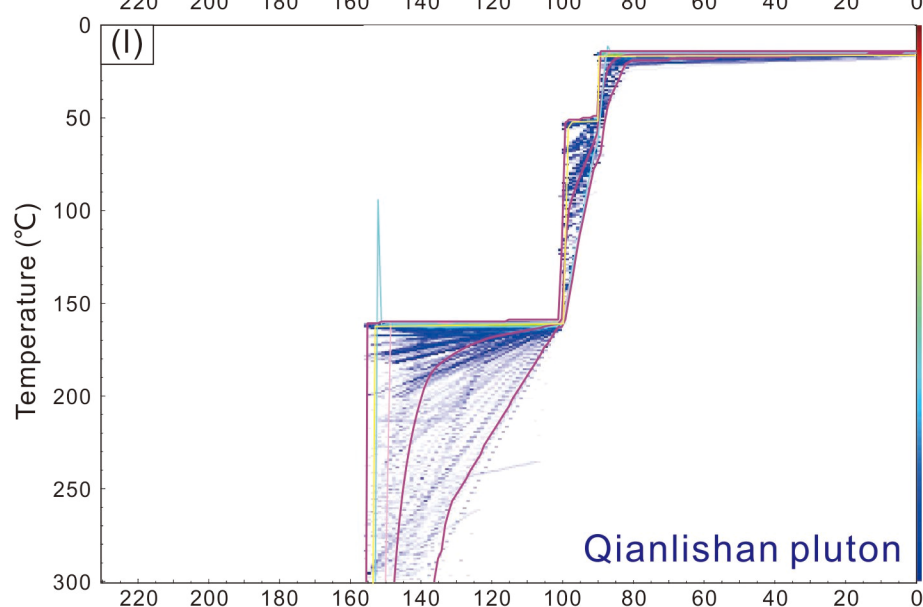
(l)
Qianlishan pluton
Temperature (℃)

Figure 7.

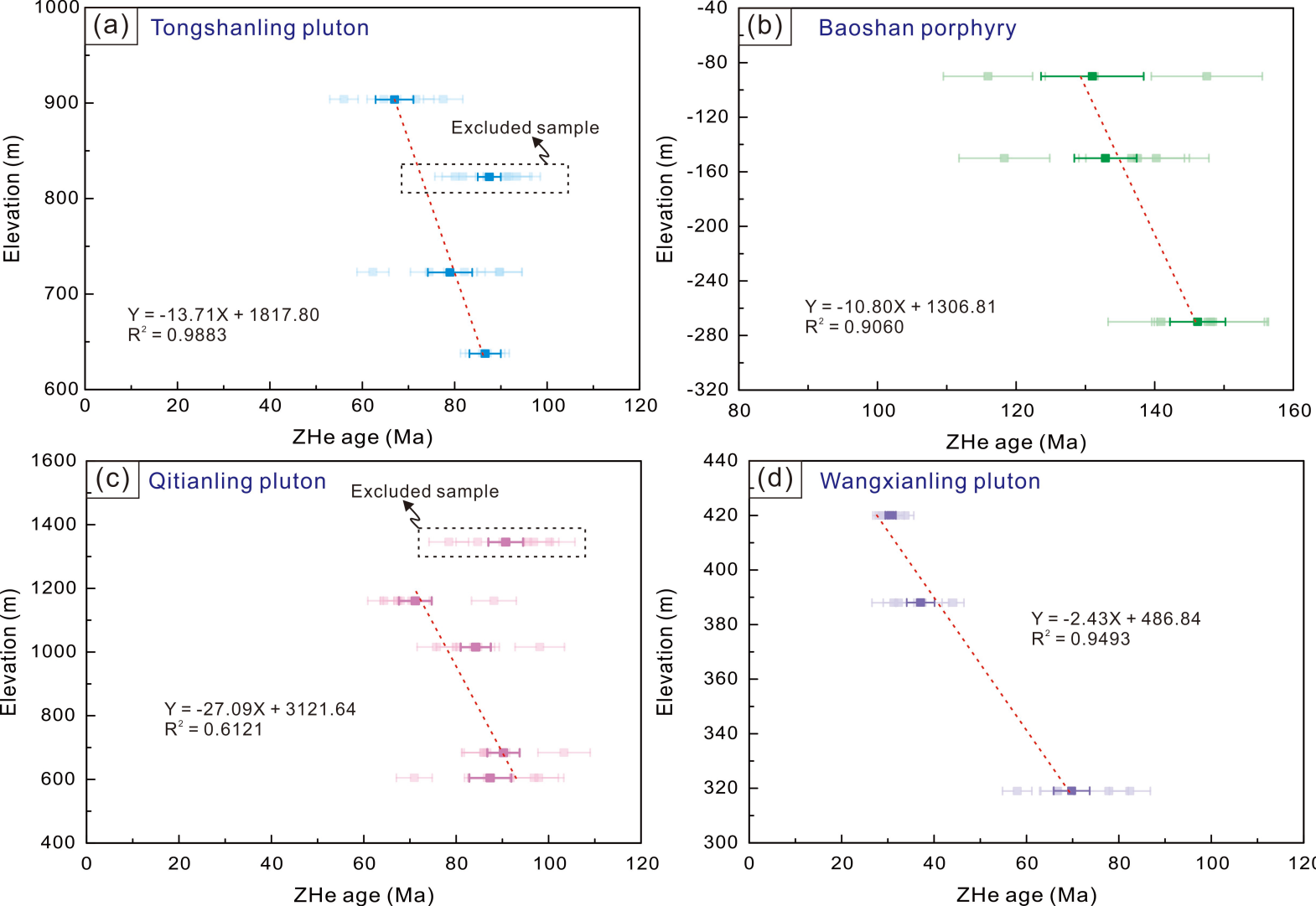
(a)
Tongshanling pluton
Excluded sample
Y = -13.71X + 1817.80
R² = 0.9883
Elevation (m)
ZHe age (Ma)
(b)
Baoshan porphyry
Y = -10.80X + 1306.81
R² = 0.9060
Elevation (m)
ZHe age (Ma)
(c)
Qitianling pluton
Excluded sample
Y = -27.09X + 3121.64
R² = 0.6121
Elevation (m)
ZHe age (Ma)
(d)
Wangxianling pluton
Y = -2.43X + 486.84
R² = 0.9493
Elevation (m)
ZHe age (Ma)

Figure 8.

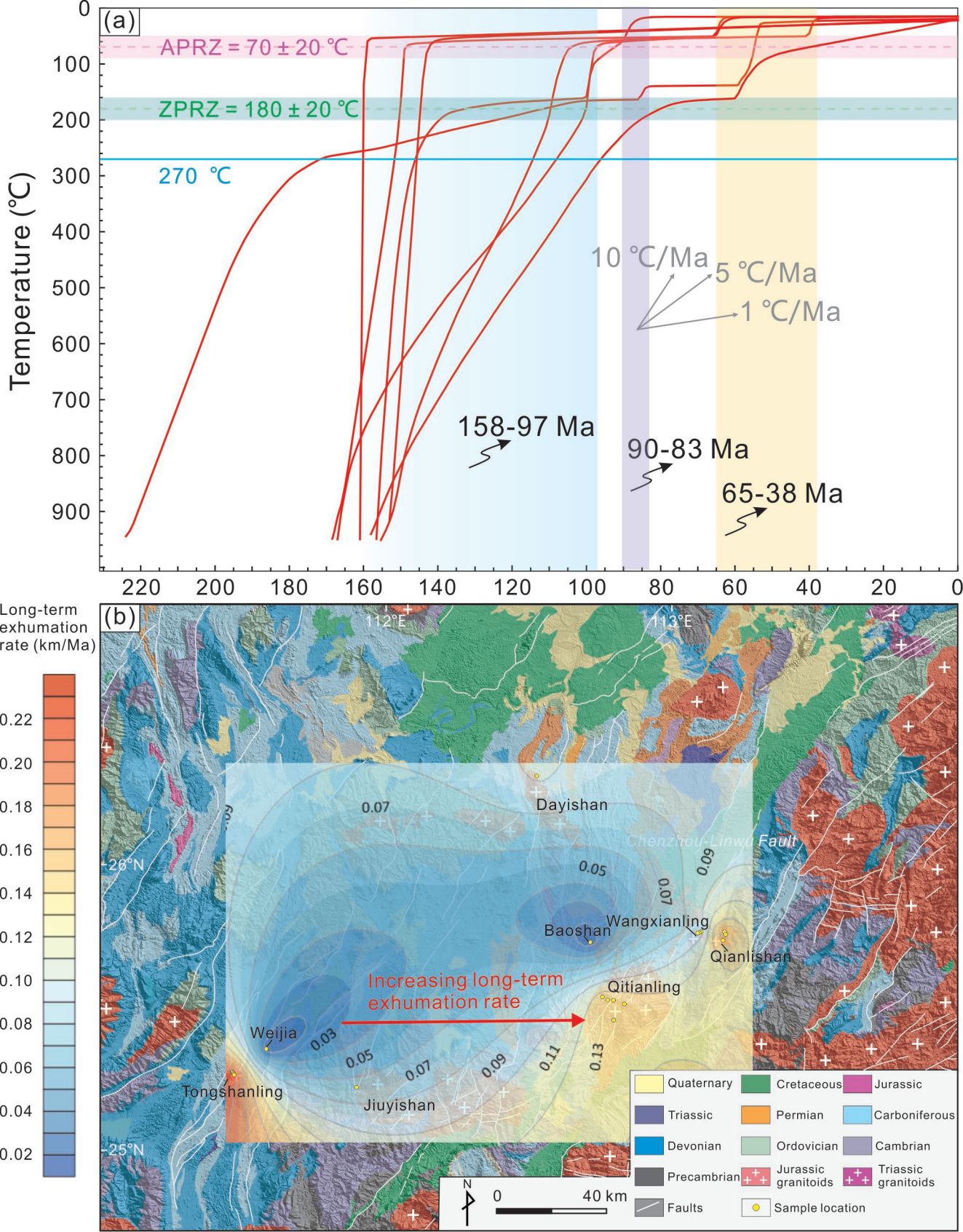
(a)
APRZ = 70 ± 20 ℃
ZPRZ = 180 ± 20 ℃
270 ℃
10 ℃/Ma
5 ℃/Ma
1 ℃/Ma
158-97 Ma
90-83 Ma
65-38 Ma
Temperature (℃)
0
100
200
300
400
500
600
700
800
900
220
200
180
160
140
120
100
80
60
40
20
0
(b)
Long-term exhumation rate (km/Ma)
0.22
0.20
0.18
0.16
0.14
0.12
0.10
0.08
0.06
0.04
0.02
112°E
113°E
26°N
25°N
Dayishan
Chenzhou-Linwu Fault
Baoshan
Wangxianling
Qianlishan
Qitianling
Increasing long-term exhumation rate
Weijia
Tongshanling
Jiuyishan
0.03
0.05
0.07
0.09
0.11
0.13
Quaternary
Cretaceous
Jurassic
Triassic
Permian
Carboniferous
Devonian
Ordovician
Cambrian
Precambrian
Jurassic granitoids
Triassic granitoids
Faults
Sample location
N
0
40 km

Figure 9.

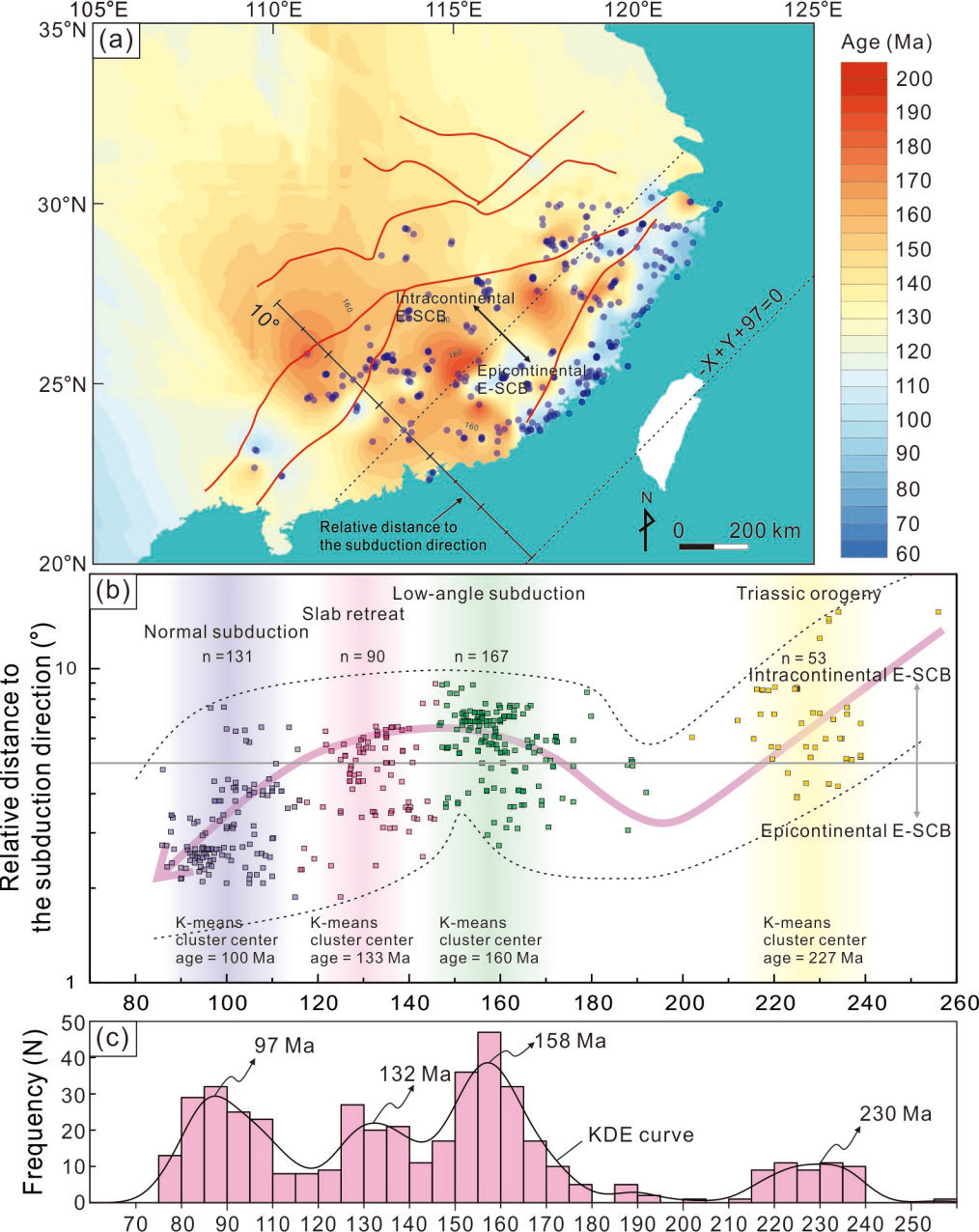
(a)
105°E
110°E
115°E
120°E
125°E
35°N
30°N
25°N
20°N
Age (Ma)
200
190
180
170
160
150
140
130
120
110
100
90
80
70
60
10°
Intracontinental E-SCB
Epicontinental E-SCB
-X+Y+97=0
Relative distance to the subduction direction
N
0
200 km
(b)
Low-angle subduction
Slab retreat
Normal subduction
Triassic orogeny
n =131
n = 90
n = 167
n = 53
Intracontinental E-SCB
Epicontinental E-SCB
Relative distance to the subduction direction (°)
10
1
K-means cluster center age = 100 Ma
K-means cluster center age = 133 Ma
K-means cluster center age = 160 Ma
K-means cluster center age = 227 Ma
80
100
120
140
160
180
200
220
240
260
(c)
Frequency (N)
50
40
30
20
10
0
97 Ma
132 Ma
158 Ma
230 Ma
KDE curve
70
80
90
110
120
130
140
150
160
170
180
190
200
210
220
230
240
250

Figure 10.

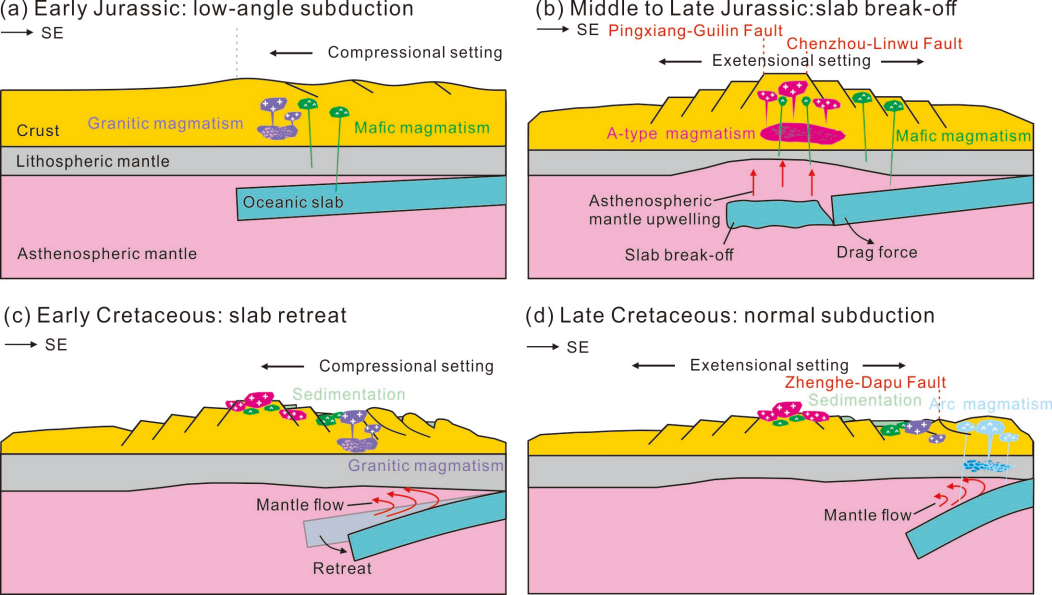
(a) Early Jurassic: low-angle subduction
SE
Compressional setting
Crust
Granitic magmatism
Mafic magmatism
Lithospheric mantle
Oceanic slab
Asthenospheric mantle
(b) Middle to Late Jurassic:slab break-off
SE
Pingxiang-Guilin Fault
Chenzhou-Linwu Fault
Exetensional setting
A-type magmatism
Mafic magmatism
Asthenospheric mantle upwelling
Slab break-off
Drag force
(c) Early Cretaceous: slab retreat
SE
Compressional setting
Sedimentation
Granitic magmatism
Mantle flow
Retreat
(d) Late Cretaceous: normal subduction
SE
Exetensional setting
Zhenghe-Dapu Fault
Sedimentation
Arc magmatism
Mantle flow

Figure 11.

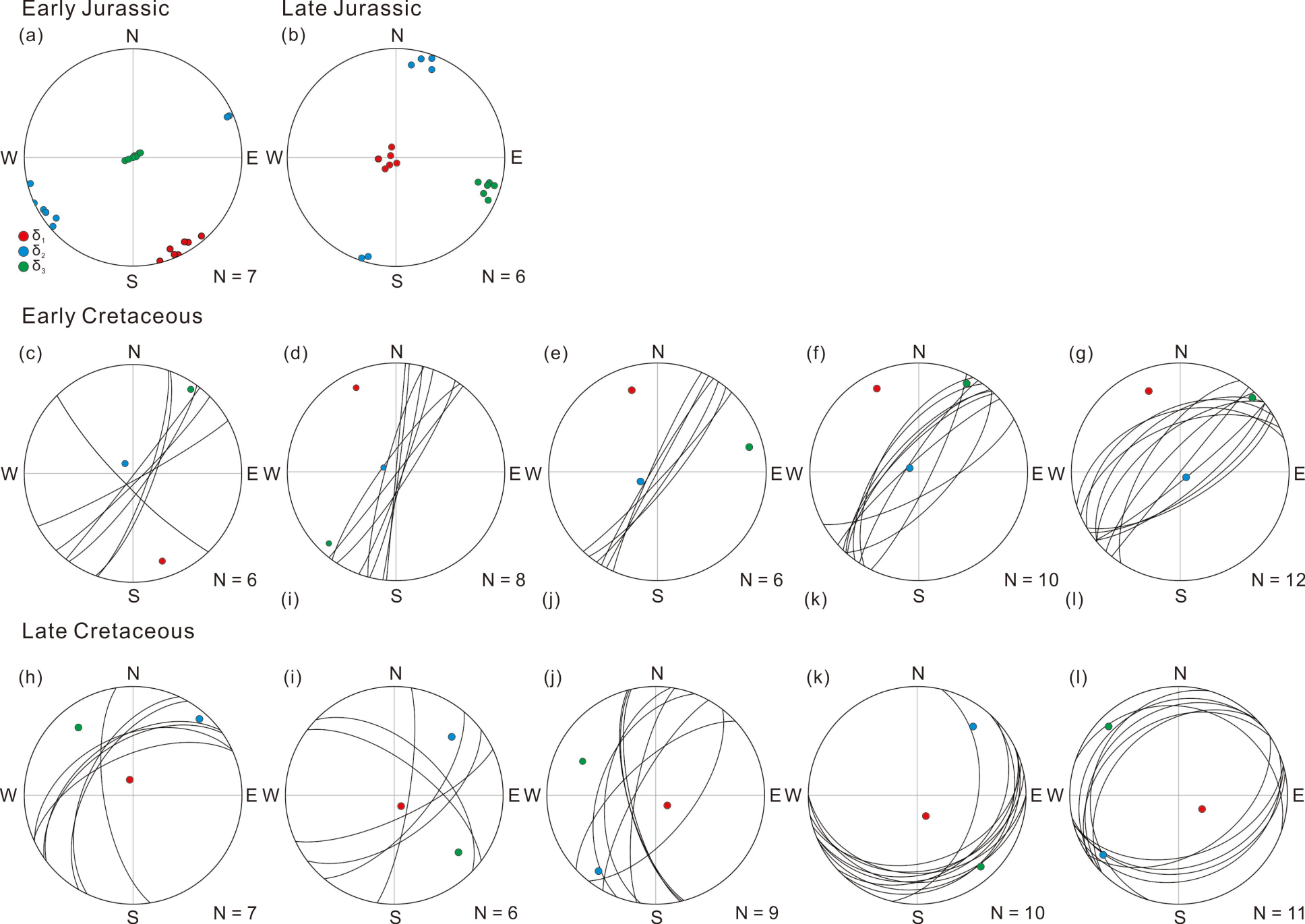
Early Jurassic
(a)
N
W
E
S
N = 7
δ1
δ2
δ3
Late Jurassic
(b)
N
W
E
S
N = 6
Early Cretaceous
(c)
N = 6
(d)
N = 8
(e)
N = 6
(f)
N = 10
(g)
N = 12
(i)
(j)
(k)
(l)
Late Cretaceous
(h)
N = 7
(i)
N = 6
(j)
N = 9
(k)
N = 10
(l)
N = 11

Figure 12.

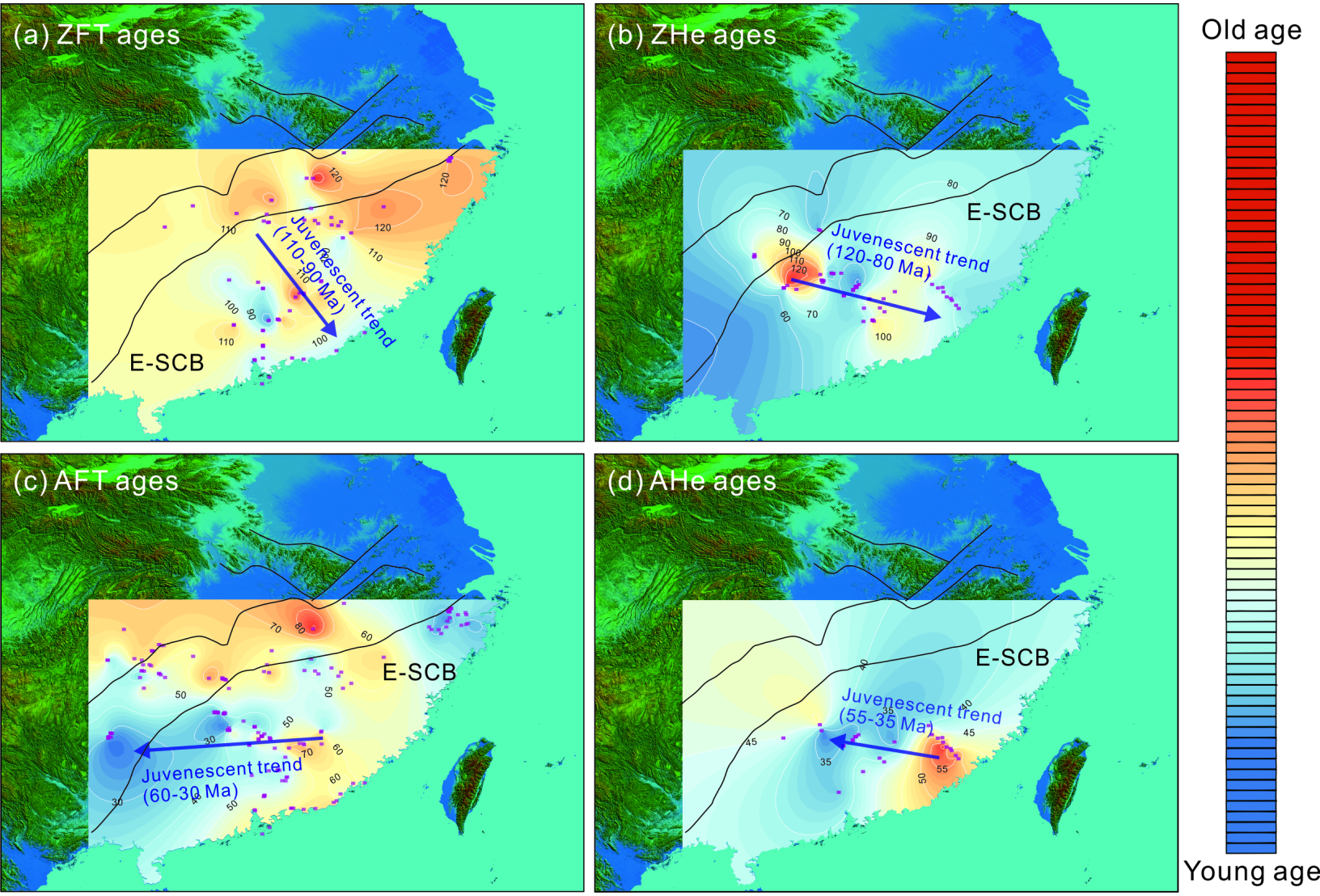
(a) ZFT ages
E-SCB
Juvenescent trend
(110-90 Ma)
(b) ZHe ages
E-SCB
Juvenescent trend
(120-80 Ma)
(c) AFT ages
E-SCB
Juvenescent trend
(60-30 Ma)
(d) AHe ages
E-SCB
Juvenescent trend
(55-35 Ma)
Old age
Young age

Table 1. Sample information

Sample No.	Lithology	Elevation (m)	Latitude and Longitude	Age (Ma)
TSL-1	Granodiorite	638	25.2750°N, 111.4619°E	166.6 ± 0.4 Ma
TSL-3	Granodiorite	723	25.2722°N, 111.4644°E	(MSWD = 0.23)
TSL-4	Granodiorite	823	25.2689°N, 111.4656°E	Kong et al., 2018
TSL-6	Granodiorite	904	25.2650°N, 111.4675°E	
WJ-1	Granite porphyry	295	A drilling hole of Weijia	158.7 ± 2.3 Ma
WJ-3	Granite porphyry	195	deposit	(MSWD = 0.78)
			25.3558°N, 111.5806°E	Kong et al., 2018
JYS-7	Granite	1028	25.2211°N, 111.8953°E	153.0 ± 0.9 Ma
				(MSWD = 0.18)
				Liu et al., 2019
DYS-1	Granite	143	26.3193°N, 112.5356°E	158.2 ± 1.2 Ma
				(MSWD = 1.2)
				Zhang et al., 2021
BS-1	Granodioritic porphyry	–150	Underground tunnels of	167.0 ± 3.0 Ma
BS-2	Granodioritic porphyry	–270	the Baoshan deposit	(MSWD = 1.12)
BS-3	Granodioritic porphyry	–110	25.7300°N, 112.7144°E	Kong et al., 2018
QTL-1	Granite	684	25.5381°N, 112.7564°E	153 ± 2 Ma
QTL-2	Granite	1016	25.5275°N, 112.7753°E	(MSWD = 0.32)
QTL-5	Granite	1161	25.5269°N, 112.7961°E	Shu et al., 2011
QTL-6	Granite	1346	25.5136°N, 112.8342°E	
QTL-7	Granite	605	25.4567°N, 112.7967°E	
WXL-1	Granite	319	25.7744°N, 113.1339°E	223.5 ± 1.8 Ma
WXL-5	Granite	388	25.7708°N, 113.1042°E	(MSWD = 0.29)
WXL-6	Granite	420	25.7706°N, 113.1019°E	Zhang et al., 2015
QLS-1	Granite	276	25.7672°N, 113.1619°E	155 ± 2 Ma
QLS-2	Granite	347	25.7575°N, 113.1657°E	(MSWD = 1.19)
QLS-3	Granite	411	25.7368°N, 113.1564°E	Shu et al., 2011

Table 2. Inverse modelling strategies for the investigated plutons

Samples	(U-Th)/He age span (Ma)		Samples for inverse modelling		Time-temperature constraints
	Zircon	Apatite	Zircon	Apatite	
Tongshanling	56–93	37–60	TSL3-3	TSL3-6	950 ± 50 ℃ for 167 ± 1 Ma 180 ± 20 ℃ for 75 ± 25 Ma 70 ± 20 ℃ for 50 ± 15 Ma
Weijia	83–162		WJ1-3 WJ3-4		950 ± 50 ℃ for 159 ± 2 Ma 180 ± 20 ℃ for 120 ± 45 Ma
Jiuyishan	97–141		JYS7-5		950 ± 50 ℃ for 153 ± 1 Ma 180 ± 20 ℃ for 120 ± 25 Ma
Dayishan	44–56		DYS1-4		950 ± 50 ℃ for 158 ± 1 Ma 180 ± 20 ℃ for 50 ± 10Ma
Baoshan	116–148	42–63	BS2-6	BS2-4	950 ± 50 ℃ for 167 ± 3 Ma 180 ± 20 ℃ for 130 ± 20 Ma 70 ± 20 ℃ for 50 ± 15 Ma
Qitianling	64–103	26–36	QTL2-1	QTL2-1	950 ± 50 ℃ for 153 ± 2 Ma 180 ± 20 ℃ for 85 ± 25 Ma 70 ± 20 ℃ for 30 ± 10 Ma
Wangxianling	28–82		WXL1-1 WXL5-5 WXL6-3		950 ± 50 ℃ for 224 ± 2 Ma 180 ± 20 ℃ for 55 ± 30 Ma
Qianlishan	77–96	75–89	QLS1-4	QLS1-3	950 ± 50 ℃ for 155 ± 2 Ma 180 ± 20 ℃ for 85 ± 15 Ma 70 ± 20 ℃ for 80 ± 10 Ma

Table 3. Calculated parameters and results of long-term exhumation rates

Granitoids	Timing of cooling phase (Ma)		Multi-phase cooling rates (°C/Ma)		Calculated long-term exhumation rates (km/Ma)	
	Stage 1 Stage 3 Stage 5	Stage 2 Stage 4	Stage 1 Stage 3 Stage 5	Stage 2 Stage 4	Inverse modelling method	Zircon-apatite method
Tongshanling	108–97 65–61	97–65	18 7.5	0.63	0.177–0.266	0.107–0.149
Weijia	158–0		0.25		0.008–0.013	
Jiuyishan	146–142	142–0	50	0.35	0.057–0.086	
Dayishan	96–80 60–0	80–60	5.6 2.3	1.0	0.087–0.130	
Baoshan	66–63		10		0.016–0.024	0.038–0.054
Qitianling	114–100 41–39	100–41	15 15	0.34	0.111–0.167	0.069–0.095
Wangxianling	172–102 86–82 59–52	102–86 82–59	1.5 5 16	0.25 0.23	0.068–0.102	
Qianlishan	146–133 100–86	133–100	6.9 10	0.61	0.139–0.208	0.800–1.114